Oscillator Based Readout System For Inductively Coupled Stretchable Resistive Strain Sensor

Billy Sixten Mårtensson
bi2401m-s@student.lu.se

Department of Electrical and Information Technology
Lund University

Supervisor: Baktash Behamanesh

Examiner: Pietro Andreani

August 28, 2023

Printed in Sweden
Tryckeriet i E-huset, Lund

Abstract

The development and use of stretchable electronics is a relatively new research field. However, the use of these kinds of electronics could prove fruitful when seeking to improve medical sensors and equipment. Since the substrates and manufacturing methods used when making stretchable electronics allows them to be extremely thin, with a thickness in the μm range. At these thickness levels, the electronics are capable of following and adhering to human skin as it bends and stretches.

This project proposes a wireless and stretchable reader and sensor system which uses a simple oscillator circuit with an inductively coupled resonator to detect resisitve strain in a fully stretchable RLC sensor circuit. By delving into the malleable nature of these cutting-edge electronics, we determine the most effective circuit parameters to optimize signal behavior for specific applications. The findings showed that the simulated frequency shift sensitivity to variations in sensor resistance in a simple NIC based oscillator circuit could (in some cases) be accurately modelled. The simulation was then confirmed via measurement with a reader circuit inductively coupled to a stretchable sensor. Further resistive strain experiments revealed a frequency shift of -0.129% per 1% of strain in the sensor resistor, which was high enough to detect the relatively faint skin deformation caused by a pulse wave from the heart. The system was then further capable of measuring the heart rate of a person which was verified using a photoplethysmography sensor.

Popular Science Summary

The modern developed world has seen tremendous improvement in healthcare over the last few decades. Better medical treatments and medicine as well as the world's effort in combating diseases has increased the average life expectancy of humans a significant amount [1]. But with an ever aging population comes new challenges. The need for monitoring people's physical values, such as heart rate and breathing without impeding a person's everyday life brings with it the need for more sophisticated measuring equipment. For example, if a person needs constant monitoring of their heart rate or continuous ambulatory electrocardiography (ECG), the person could in many cases be confined to a bed or he/she might be connected to bulky medical equipment. This could impede a person's movement and severely affect their quality of life. Advancement in wireless power transfer (WPT) technology [2] and the development of stretchable electronics [3] could prove to be of great benefit when developing new medical sensory technology. Firstly, the wireless sensor allows for the reading of the sensor without a physical restraints, such as connected wires. This makes it possible to integrate the readers in clothing which a person can easily move in or remove as needed. Secondly, sensors constructed with stretchable electronics can be made very thin such that they can conform to the human skin as well as follow the stretching and bending of the skin as a person moves. These kinds of sensor would apply no external strain on the skin or body and they are very soft which makes them a lot more comfortable to wear than sensors made from rigid electronics. The use of wireless technology in sensors, or the combination with stretchable electronics is not an entierly new concept and has been successfully implemented before [4]. This thesis project aims to investigate the behavior and sensitivity of inductively coupled stretchable resistive strain sensors. The goal is to find the most beneficial circuit topologies and circuit parameters for constructing a reader sensor system sensitive enough to detect physical signals and phenomena such as heart rate, breathing and movement. The system will be both simulated using software and a physical reader and sensor will be constructed and evaluated for performance.

Table of Contents

List of Figures

List of Tables

Chapter 1
Introduction

1.1 Background

In the modern world, the tracking of physiological values such as blood pressure, heart rate and movement are becoming more common. The tracking of physiological values are of both importance and interest in areas such as healthcare where they are used to monitor the health of patients and in sports where they can be used to analyze an athlete's performance. Furthermore, we live in a society with an ever aging population and with that comes a growing need for more sophisticated medical equipment. In some cases, a patient may even need constant surveillance of their physiological values. This could severely affect a person's quality of life, either by confining them to a bed or impeding their movement by being connected to uncomfortable measuring equipment. Recent development of ultrathin and stretchable materials could prove beneficial in this area. Electrical components such as resistors, inductors, capacitors, diodes and transistors (to name a few) have been developed using ultrathin and stretchable materials [5][6][7][8]. But how would ultrathin and stretchable materials be of benefit when developing sensors? Well, ultrathin materials have the inherent ability to conform to a person's body. The human skin contains many microscopic groves and wrinkles, but, since ultrathin substrates can have a thickness in the μm range it can follow the skin surface [9]. Additionally, when a person moves, the skin will stretch and deform. A substrate that is stretchable in addition to being ultrathin, would therefore be able to follow the skin's movement and deformation without causing discomfort or friction to the skin itself. When, for example, taking conventional ECG measurements, rigid electrodes are used. These electrodes would not stay attached to the patient's body if they were to move and do many of our daily activities such as exercising or showering. I.e, conventional ECG measurement would impede a person's movement. If instead the patient in question would be connected to electrodes made from ultrathin substrate, this impediment could be drastically lessened.

The next improvement one could think of when it comes to taking physiological measurements is how to acquire the data. Traditionally, such measurements would be obtained via physical wires connected to the sensor itself. There has of course been research made into acquiring this kind of physiological data in a wireless manner. Photoplesmography (PPG) is one such method [10]. In PPG, blood

vessels absorb light via irradiation from a controlled light source and then re-emits the light which is measured with a photosensor. In this way, a person's heart rate can be measured "wirelessly". PPG is a common technology in, for example smartwatches [11]. Another method is via electromagnetic coupling between a reader and sensor circuit. Here, small perturbations in the sensor circuit can affect the energy transference between the reader and the sensor. These changes can then be detected and measured by the reader [12]. I.e, physical phenomena in a person's body can affect the characteristics of a sensor and then be wirelessly measured by a reader.

So how would one go about wirelessly acquiring data from the aforementioned ultrathin and stretchable sensor? One way is via the previously mentioned electromagnetic coupling. As mentioned before, a number of different circuit components can be constructed with stretchable materials. This means that an RLC circuit can be constructed. Such an RLC circuit can then be interrogated using an inductor coil connected to a reader circuit, in this way the reader can detect changes in the stretchable sensor.

1.2 Motivation

The use of stretchable circuit components come with their own challenges. The capability to deform that is inherent to all circuit components, also means that they will change their parameter values (resistance, capacitance and inductance) when said deformation occurs [4]. Picture for example a sensor patch that is placed on a person's wrist, the patch is oriented so that the resistor in the RLC circuit is placed over an artery so that it will be deformed when a pulse wave from the heart passes through the artery. The deformation of the resistor will cause a change in the signal detected by the reader. In this way, heartbeat can be measured. But, if the person were to move his/hers wrist, the inductor coil in the circuit would also deform. This could, in turn, also cause additional variations in the signal detected by the reader. It is therefore evident that multiple actions, voluntary or involuntary, by the person can induce a change in the characteristics of multiple sensor components. In order to make a robust and reliable reader system for fully stretchable sensors, a method or model is needed to determine the behavior of stretchable circuits and additionally if possible distinguish between changes in the different components. Previous research has been directed towards estimating multiple parameters [13], however, to our knowledge, it has never been made for fully stretchable sensors.

1.3 Goal

The goal of this thesis is firstly to estimate the frequency behavior and sensitivity of a wireless and stretchable sensor when variations in the different components occur. And secondly to construct a reader circuit for a stretchable resistive strain sensor. To achieve this, the focus of this thesis will be to:

- Find an equivalent circuit for a wireless power transfer system.

- Construct and simulate the circuit in the software LTspice.
- Design a PCB circuit to test the functionality of the proposed circuit.
- Evaluate the sensitivity of the system by measuring resistive strain.

1.4 Report Structure

The remaining 4 chapters are structured as follows: Chapter 2 gives the theoretical framework of this project. Chapter 3 describes the simulations and experimental setup used to test and evaluate the system. Chapter 4 gives and discusses the results from simulations and experimental measurements. Chapter 5 presents the conclusion and discussion of the thesis.

Chapter 2

Theoretical Framework

This chapter gives a theoretical explanation for the various components and theories used in this thesis.

2.1 Circuit Topologies

There are four common topologies for RLC based wireless power transfer (WPT) systems: series-series (SS), series-parallel (SP), parallel-parallel (PP) and parallel-series (PS) (see Figure 2.1). A lot of research has been directed towards finding the optimal topology in WPT systems for biocompatible implants [14, 15, 16, 2, 17]. However, this research is often intended for wireless charging which aims to maximize power transference and signal stability and is not necessarily the goal when making sensitive sensors. Then the circuit topologies used in sensor systems are then of more importance [18, 19, 20, 21]. The SS and SP topology are often used in which an oscillator or function generator drive the LC tank. An example of the SS-topology circuit for wireless readout of resitive strain sensor can be seen in Figure 2.2. If the oscillator and buffer in Fig.2.2 is replaced by an NIC as in this project, no oscillation would start since C_1 would block the DC supplied by the NIC. This limits the possible topologies to either PP or PS.

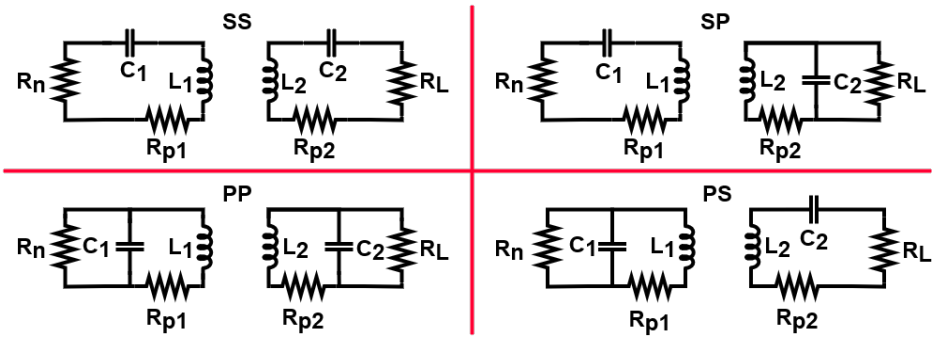

Figure 2.1: Circuit topologies for RLC based WPT systems.

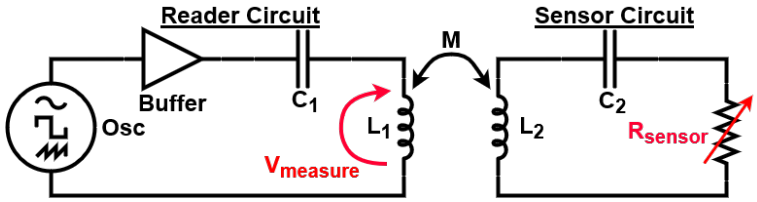

Figure 2.2: Inductive coupling wireless readout circuit of resistive strain sensor.

2.2 Coupled Mode Theory

Coupled mode theory (CMT) can be used to represent the energy in a WPT system. The energy can be described by the following equations [12]:

$$\frac{\delta a_1}{\delta t} = (j\omega_1 + g)a_1 - jK_{12}a_2 \tag{2.1}$$

$$\frac{\delta a_2}{\delta t} = (j\omega_2 - \tau)a_2 - jK_{21}a_1 \tag{2.2}$$

where a_n are the energies in the system, ω_n is the normal angular oscillation frequency of the reader and the sensor respectively, g is the gain factor in the reader and τ is the loss factor in the sensor. $K_{12} = \omega_2 k/2$ and $K_{21} = \omega_1 k/2$ are coupling rates. Writing $a_n = A_n e^{j\omega t}$ and $\delta a_n/\delta t = j\omega A_n e^{j\omega t}$, eq 2.1 and 2.2 can be solved for the angular oscillation frequency as the following:

$$\omega = \omega_f \pm \sqrt{\omega_f^2 - \omega_1\omega_2 - j(g\omega_2 - \tau\omega_1) - g\tau + K_{12}K_{21}} \tag{2.3}$$

where $\omega_f = (\omega_1 + \omega_2 + j(g - \tau))/2$. If the system components are chosen so that $g = \tau$ and $\omega_1 = \omega_2 = \omega_0$ the complex components in eq 2.3 disappears and the following equation can be used to describe the angular oscillation frequency of the system:

$$\omega = \omega_0 \pm \sqrt{K_{12}K_{21} - g\tau} \tag{2.4}$$

The gain and loss factors are different in different circuit topologies and since the PP and PS-topologies are the only relevant ones as stated in section 2.1, these are the only ones that are presented in Table 2.1. From Table 2.1 and eq 2.4 it is

Topology	*Gain Factor*	*Loss Factor*
PS	$g = \frac{1}{2R_nC_1} - \frac{R_{p1}}{2L_1}$	$\tau = \frac{R_{p2}}{2L_2} + \frac{R_{sensor}}{2L_2}$
PP	$g = \frac{1}{2R_nC_1} - \frac{R_{p1}}{2L_1}$	$\tau = \frac{R_{p2}}{2L_2} + \frac{1}{2R_{sensor}C_2}$

Table 2.1: Gain and loss factor in the PS and PP topologies.

clear that the sensor resistance R_{sensor} affects on the oscillation frequency.

2.3 Stretchable Electronics

Stretchable electronics can be made using various materials, structures and manufacturing methods. Stretchable metal conductors are often constructed using gold (Au) and silver (Ag) since they have high conductivity. Organic conductors can be made using poly(3,4-ethylenedioxythiophene) polystyrene sulfonate (PEDOT:PSS) [6] and oxide conductors can be made with indium tin oxide (ITO) [22] and indium zinc oxide (IZO) [23]. Other usable stretchable conductors can be carbon based such as carbon black, carbon-nanotubes and graphene [3]. Stretchable dielectrics can be made using polystyrene-block-poly(ethylene-ran-butylene)-block-polystyrene (SEBS) [8]. Stretchable semiconductors can be constructed using for example, poly(3-hexylthiophene-2,5-diyl) nanofibrils (P3HT-NFs) and Polydimethylsiloxane (PDMS) [24]. Common architecture for stretchable conductors include, composites, liquid metals and structure-based conductors.

Composites are constructed by mixing an elastomer like PDMS with a conductive powder like Au powder, Ag powder or carbon (C) powder. It is done by implanting the conductive powder until the "percolation threshold" is reached, after which the conductivity of the elastomer increases rapidly until it reaches the bulk conductivity. By increasing the amount of conducting powder in the elastomer, the likelihood that electron tunneling occurs increases and thereby the conductivity of the material. At the same time there is no rigid connection between the conductive powder, meaning that the stretchability of the elastomer remains.

The liquid metals used in stretchable conductors/circuits are metals or metal alloys that remain liquid at room temperature. One such metal alloy is gallium-indium (GaIn) [25], when mixed with a ratio of Ga:In=3:1 it remains in a liquid state at $15.7°C$ [26] and has a conductivity of $3.4x10^6$ S/m. Liquid metals can be painted, sprayed or applied with some other method to an elastomer substrate to form a circuit, a second layer of elastomer can then be added on top of the substrate in order to incase an insulate the circuit. This way a stretchable circuit is created that retains its original shape even after it is strained and relaxed. Self-healing circuits have been successfully constructed and demonstrated using liquid metals. The stretchable circuit used in this project is partially made with liquid metal.

The third method used to make stretchable conductors/circuits is with structure-based methods. This entails forming the conductors in different "non-straight" shapes. Serpentine structure means that the conductive layer is applied to the elastomer in a serpentine manner that becomes straight lines and does not break the connection if the elastomer is stretched. Accordion structure can be formed by first stretching the elastomer and then applying the conductive layer. When the elastomer is relaxed, the conductive layer forms waves that can later be stretched. Microcracks can be formed by controlling the conditions (for example deposition speed) when applying the conductive layer so that it forms many small cracks in the conductive layer. When the elastomer is stretched the cracks open up while conductive traces remain in the conductive layer. Microcrack technology is another method used in the manufacturing of the stretchable sensors used in this project.

The above mentioned stretchable conductors are of course not infallible and

all are limited by the elastomer or architecture used. The stretchability of the conductors/circuits have been shown to vary form 10% to 1000%. [27]

2.3.1 Strain Sensitivity

When analyzing a stretchable RLC sensor, the sensitivity that each component displays when subjected to strain needs to be established. To this end, previous data was used for the sensor resistance (R_{sensor}). R_{sensor} made of Au using an evaporation rate of 0.5 Å/s showed an increase in resistance of ca 900% at a 120% strain, or ca 7.5% increase in resistance for every 1% of strain [28]. The sensor capacitance (C_2) is constructed as a plate capacitor and can be expected to increase relatively linear with strain as the area (A) increases according to $C = \epsilon_0 \epsilon_r A/d$ where ϵ_0 is the electric constant, ϵ_r is the relative permittivity of the material between the plates and d is the separation distance between the plates. I.e, C_2 would increase ca 1% for every 1% of strain. For the sensor inductance (L_2) sensitivity, measurements were made using a prototype stretchable planar coil. It increased by 6.1% at 25% strain or 0.24% for every 1% of strain. When the inductor coil is stretched horizontally, the distance between the vertical traces increases. However, at the same time the inductor contracts in the vertical direction and the distance between the horizontal traces decreases. For this reason the inductance does not change at a ratio of 1:1.

2.4 Transformer Circuit Analysis

A system that transfers energy wirelessly via electromagnetic coupling can be viewed as a simple transformer circuit with an air core as seen in Figure 2.3. The

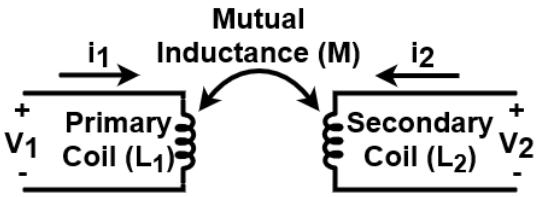

Figure 2.3: Figure of transformer circuit with an air core.

KCL equations for the transformer can be written as

$$V_1 = L_1 \frac{di_1}{dt} + M \frac{di_2}{dt} \tag{2.5}$$

$$V_2 = L_2 \frac{di_2}{dt} + M \frac{di_1}{dt} \tag{2.6}$$

in the time domain, and

$$V_1 = j\omega L_1 i_1 + j\omega M i_2 \tag{2.7}$$

$$V_2 = j\omega L_2 i_2 + j\omega M i_1 \tag{2.8}$$

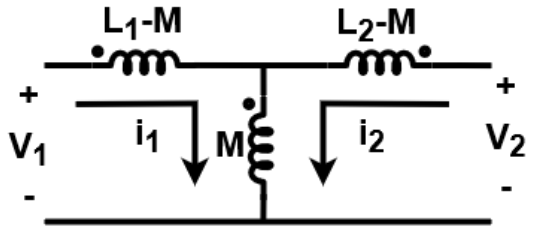

Figure 2.4: Figure of the T-equivalent circuit.

in the frequency domain. The circuit in Figure 2.3 can be redrawn as a T-equivalent circuit as seen in Figure 2.4 where $i_1 + i_2 = i_3$. By using KCL on the circuit in Figure 2.4 the following equations can be derived

$$V_1 = (L_1 - M)\frac{di_1}{dt} + M\frac{d(i_1 + i_2)}{dt} = L1\frac{di_1}{dt} + M\frac{di_2}{dt} \tag{2.9}$$

$$V_2 = (L_2 - M)\frac{di_2}{dt} + M\frac{d(i_1 + i_2)}{dt} = L_2\frac{di_2}{dt} + M\frac{di_1}{dt} \tag{2.10}$$

in the time domain, and

$$V_1 = j\omega(L_1 - M)i_1 + j\omega M(i_1 + i_2) = j\omega L_1 i_1 + j\omega M i_2 \tag{2.11}$$

$$V_2 = j\omega(L_2 - M)i_2 + j\omega M(i_1 + i_2) = j\omega L_2 i_2 + j\omega M i_1 \tag{2.12}$$

in the frequency domain. By comparing equations 2.5 and 2.6 with equations 2.9 and 2.10 it is evident that the circuits behaves the same in the time domain. Similarly by compare equations 2.7 and 2.8 with equations 2.11 and 2.12, the two circuit behaves the same in the frequency domain as well. It can therefore be concluded that the T-equivalent circuit in Figure 2.4 is equivalent to the transformer circuit in Figure 2.3.

2.5 Mutual Inductance

When working with energy transference between two inductor coils, two very important parameters are the mutual inductance "M" between the coils and the coupling factor "k". These two parameters relate to each other according to the following equation:

$$k = \frac{M}{\sqrt{L_1 L_2}} \tag{2.13}$$

where L_1 is the self inductance of the primary or reader coil and L_2 is the self inductance of the secondary or sensor coil. The coupling factor describes the flux leakage between the two coils where k=1 is no flux leakage and k=0 is 100% flux leakage. However, in reality, $k < 1$. The mutual coupling factor and/or the mutual inductance is affected by various parameters, among others, the geometric shape of the coils and the distance between the coils [29]. The mutual inductance of two coils can be calculated by measuring the inductance of the configurations in Figure

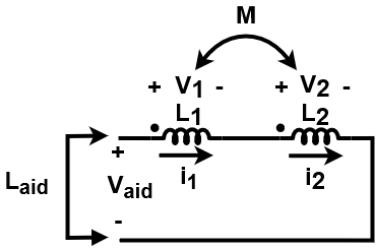

Figure 2.5: Series-aiding inductance

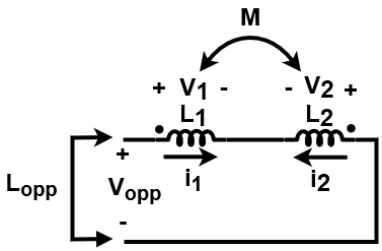

Figure 2.6: Series-opposing inductance.

2.5 and 2.6. The first thing to note is that equations 2.11 and 2.12 can be used to describe the circuits in Figure 2.5 and 2.6. Furthermore, by analysing Figure 2.5, one can see that $i_1 = i_2$, $V_{aid} = V_1 + V_2$ and $V_{aid} = i_1 \cdot j\omega L_{aid}$. Combining these expressions with equations 2.11 and 2.12, the following expression can be found:

$$L_{aid} = L_1 + 2M + L_2 \tag{2.14}$$

Next, in Figure 2.6 one finds the following expressions, $i_1 = -i_2$, $V_{opp} = V_1 - V_2$ and $V_{opp} = i_1 \cdot j\omega L_{opp}$. Performing the same operation as with the last expressions gives the following.

$$L_{opp} = L_1 - 2M + L_2 \tag{2.15}$$

Lastly by setting equation 2.14 equal to equation 2.15, the following equation for mutual inductance is found.

$$M = \frac{L_{aid} - L_{opp}}{4} \tag{2.16}$$

The spiral planar coils in Figure 2.11 and 2.12 were used to measure the aiding and opposing inductance in accordance with Figure 2.5 and 2.6. The following combinations of coils were measured while varying the separation distance from 0 mm to 38 mm: square to stretchable coil, square to square coil, square to hexagonal coil and hexagonal to hexagonal coil. Equation 2.13 and 2.16 were then applied to calculate the mutual inductance and subsequently the coupling factor. Figure 2.7 presents the resulting coupling factor as a function of separation distance.

2.6 Planar Coils

In this work, spiral planar coil inductors were used to establish the inductive coupling between the reader and sensor circuits. Spiral planar coils, as the name suggests are designed as parallel metal traces going in a spiral formation and can have numerous designs, such as square, hexagonal, circular and so on. The inductance of a spiral coil is given by both the self inductance of each trace "L_i" and the mutual inductance between the traces "M_{ij}". The square spiral coil in Figure 2.8 can be viewed as four traces, AB, BC, CD and DE with the respective

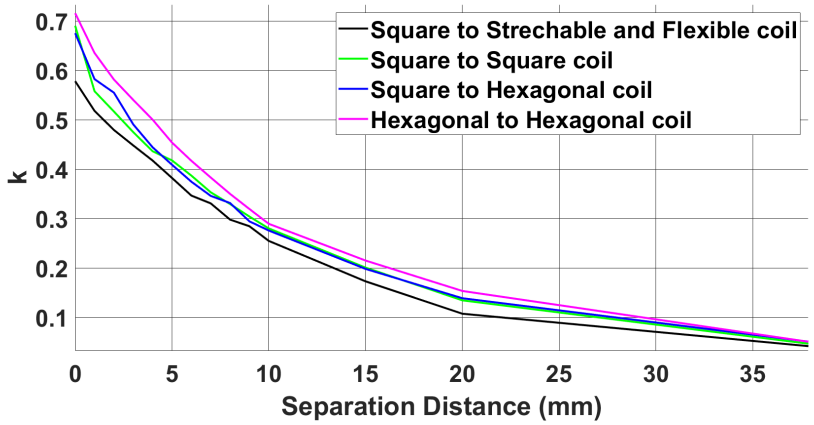

Figure 2.7: Coupling factor for different coil combinations at varying separation distance.

inductances L_1, L_2, L_3 and L_4. Adding the trace inductances to the mutual inductances the following equation for the total coil inductance can be derived:

$$L_{tot} = L_1 + L_2 + L_3 + L_4 + M_{12} + M_{13} + M_{14} + M_{23} + M_{24} + M_{34} \tag{2.17}$$

The second important "feature" of a spiral planar coil inductor is its internal parasitic capacitance. All the partitions between the metal traces form capacitors which can add up to a significant parasitic capacitance. This parasitic capacitance and the total coil inductance will form its own LC tank with its own self-resonance frequency (f_{sr}). At f_{sr} the inductance and capacitance cancel each other out and the LC tank is reduced to just the parasitic resistance of the coil, i.e, f_{sr} is the maximum resonance frequency at which the coil can oscillate and should be considered when deciding the operation parameters for a system. The equivalent parasitic capacitance "C_{eq}" can be found by first calculating the capacitance "C_i" between each metal trace in Figure 2.9, for example between BC and FG using the equation for capacitance:

$$C_i = \epsilon_0 \epsilon_r \frac{A_i}{d_i} \tag{2.18}$$

where $\epsilon_0 = 1/(36\pi)\cdot 10^{-9} F/m$ is the electric constant, ϵ_r is the relative permittivity of the material between the trances, A is the overlapping area of the traces and d is the separation distance between the traces. Next, C_{eq} can be approximated as:

$$C_{eq} \approx \frac{1}{K}\frac{1}{n}\sum_{i=1}^{n} C_i \tag{2.19}$$

where "K" is the number of traces in the spiral coil and "n" are the number of individual capacitors. [30]

An online tool [31] was used to create rough design parameters for a square and hexagonal spiral planar coil with the estimated inductance of 783 nH and 803

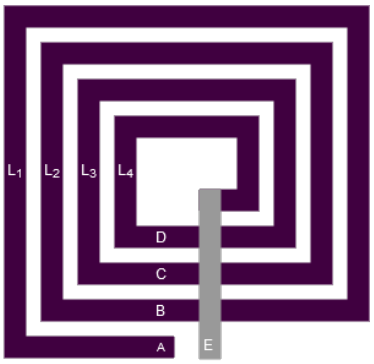

Figure 2.8: Model for visualizing the total inductance.

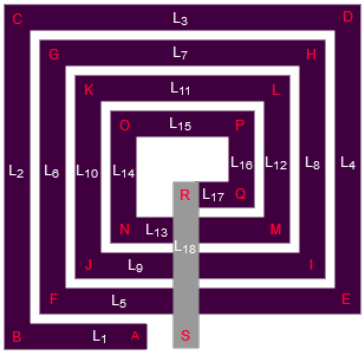

Figure 2.9: Model for visualizing the parasitic capacitance in a spiral coil.

nH respectively. The planar coils were then modeled with the software KiCad as in Figure 2.10 and later printed as FPC circuits via PCBgogo (see Figure 2.11). The inductance of each planar coil was manually measured with an LCR meter (HIOKI 3532-50 LCR HiTESTER[32]) and came out to 980.5 nH for the square coil and 1062.1 nH for the hexagonal coil. The planar coil designs were lastly sent to Matsuhisa Laboratory at the University of Tokyo where the square design was made into a stretchable coil (see Figure 2.12). The hexagonal design proved too difficult to manufacture with the available methods. The stretchable coil was also measured with the same LCR meter and showed an initial inductance of 881 nH.

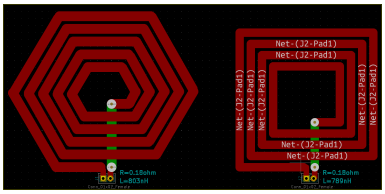

Figure 2.10: KiCad designs of spiral planar coil inductors.

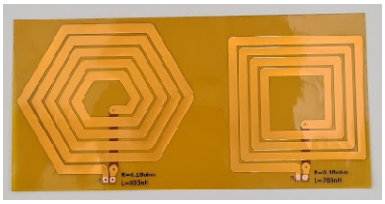

Figure 2.11: FPC spiral planar coil inductors.

The parasitic capacitance of the square FPC coil was estimated using 2.18 and 2.19. ϵ_r for the polymid material used in the FPC is between 3.0 to 4.0, both will be used in the calculations to find an upper and lower limit to the parasitic capacitance. The thickness of the coil traces is 0.1 mm, the distance between traces is in general 1 mm and the overlapping length varies. In Figure 2.9 one can see that there exists a total of 22 capacitance between the parallel traces, however, any capacitor formed with RS were extremely small and could be neglected. The same was true for the capacitors formed between NO and PQ and between OP and QR. After this filtering, only 13 capacitors remain between the 18 traces, i.e, $n = 13$ and $K = 18$. The resulting upper and lower equivalent parasitic

Figure 2.12: Stretchable coil manufactured by Matsuhisa Laboratory.

capacitance was C_{eq}=[4.56, 6.08] fF. Using these values with the measured self-inductance of the square coil in Figure 2.11, the resulting self-resonance frequency was: $f_{sr} = 1/(2\pi\sqrt{L \cdot C_{eq}}) \approx$ [2.38,2.06] GHz.

2.6.1 Parasitic Capacitance Between Planar Coils

Another factor to take into consideration when working with planar coils in close proximity is the parasitic capacitance that forms between the reader and sensor coil. If the parasitic capacitance is around the same size as the capacitance used in the LC tanks, or even larger, they can severely affect the oscillation frequency of the system and make it unpredictable. The parasitic capacitance can be approximated by first assuming that the coils are perfectly aligned and perpendicular and then measuring the entire surface area of the conducting traces that face each other. Equation 2.18 can be used to find the capacitance between the two coils. This time however there is only one capacitance (i=1) and ϵ_r is given the permittivity value for air (1.00054) and glass (5 to 10) depending on the insulator used. The total length of the traces in the square coil in Figure 2.11 were 551.25 mm and the width of the traces were 3 mm. The separation distance between the traces varied from 1 mm to 10 mm. The stretching of the sensor coil was also taken into consideration. The coil in Figure 2.12 could be stretched up to 25% without breaking and at 25% strain, only ca 80% of the coil surface area were aligned. Using all this information with equation 2.18 gives the upper and lower limit to the parasitic capacitance as shown in Figure 2.13.

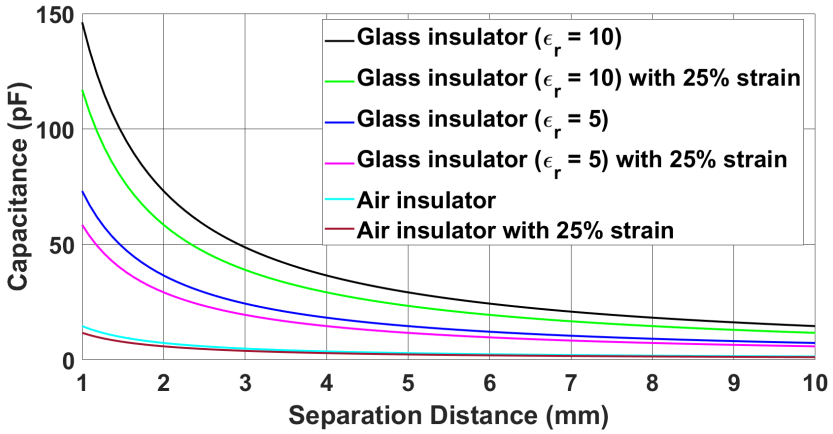

Figure 2.13: Parasitic capacitance between two square planar coils.

2.7 LC Oscillator

The LC oscillator relies on the charging and discharging of internal components in a resonator tank, that being the inductor (L) and capacitor (C). A standard LC resonator can be seen in Figure 2.14. If a charged capacitor is connected to an inductor the capacitor will start to discharge, decreasing its stored energy by sending out current and charging and increasing the stored energy within the inductor. The current increases over time which also increases the magnetic field within the inductor since the magnetic field is directly linked to the current according to Ampère's circuital law (eq 2.20):

$$\oint_C H\,\delta L = I + \int_s \frac{\delta D}{\delta t} \bullet \delta s \tag{2.20}$$

where H is the magnetic field intensity in an area encompassed by loop C, I is the current flowing through the conductor. D is the electric flux density that, when passing through a surface s, generates a displacement current that adds to the total current. A displacment current is present when the circuit isn't fully connected, for example as in the case of a capacitor. [29] When the current in the circuit has reached its maximum, the magnetic field in the inductor collapses and a current starts flowing in the opposite direction charging the capacitor. The charging and discharging can't occur indefinitely and the energy in the circuit will dissipate because of electrical friction from the parasitic resistance represented by R_p in Figure 2.15. In order to have a sustained oscillation, energy needs to be supplied to the circuit, for example via a negative impedance.

2.8 Negative Impedance Converter

The negative impedance converter (NIC) is a simple circuit constructed with a single op-amp as seen in Figure 2.16. Vb is the biasing voltage for the op-amp and

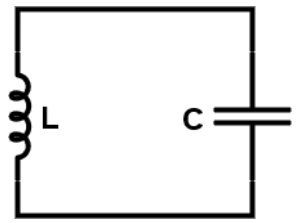

Figure 2.14: LC resonator.

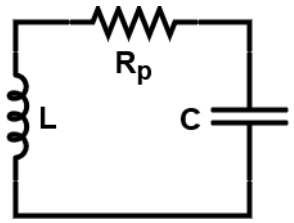

Figure 2.15: Model for visualizing R_P in a spiral inductor coil.

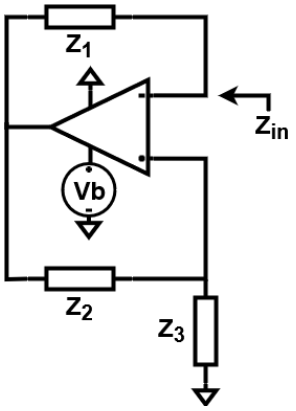

Figure 2.16: LC circuit with parasitic resistance.

Z_1 to Z_3 can be resistors, inductors or capacitors. By performing a nodal analysis of the NIC while assuming an ideal op-amp, the following negative impedance can be seen when looking into the positive port on the op-amp:

$$Z_{in} = -Z_1 \frac{Z_3}{Z_2} \tag{2.21}$$

An NIC can be used to drive an LC resonator in order to achieve continues oscillation by providing enough negative resistance to cancel out the positive resistance in the circuit.

2.9 Double Dabble

Any signal sampled by the FPGA, i.e, the oscillation frequency, will be stored in a binary format. A binary number is not something humans are used to reading and some way of translating the binary number into a readable number is needed. Additionally, the software Vivado used to program the FPGA, does not provide a graphic user interface (GUI) and some additional software or hardware is needed. With these limitations in mind, the algorithm "Double Dabble" [33] was used. Double Dabble converts a binary number into a binary-coded decimal (BCD) number. A BCD number can represent any number by encoding each separate digit with four bits (see Figure 2.17).

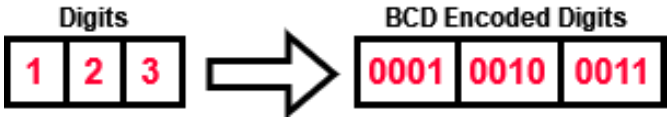

Figure 2.17: BCD encoding.

This algorithm provides a number format that is easy to use with a 7-segment display since each segment often uses four bits to represent each digit [34], the BCD format is also a convenient middle stage when converting the binary numbers into another format such as ASCII. ASCII in itself is an easy format to read and understand when utilizing universal asynchronous receiver-transmitter (UART) communication.

The double dabble algorithm can be implemented in the following way: Start with the binary number that should be converted, again 123 which is represented in binary as 1111011 and an empty register of the size four times larger than the number of digits in the binary number, i.e, the register should be of the size $4x3 = 12$ bits. The binary number will be left shifted into the empty register ones for every bit in the binary representation of the number, in this case it would be a total of seven left shifts. After each left shift, the individual 4-bit segments in the previously empty register will be checked and if any of the 4-bit segments equal to five or higher, three will be added to that segment and the left shifting will continue. The double dabble algorithm in work can be seen in Table 2.2. Since double dabble utilizes the shifting of registers and not any complex mathematical computations it is a splendid algorithm to implement in Verilog for the FPGA in this project.

Operation	*Hundreds*	*Tens*	*Units*	*Binary*
Start	0000	0000	0000	1111011
Left Shift 1	0000	0000	0001	1110110
Left Shift 2	0000	0000	0011	1101100
Left Shift 3	0000	0000	0111	1011000
Add 3 to Units	0000	0000	1010	1011000
Left Shift 4	0000	0001	0101	0110000
Add 3 to Units	0000	0001	1000	0110000
Left Shift 5	0000	0011	0000	1100000
Left Shift 6	0000	0110	0001	1000000
Add 3 to Tens	0000	1001	0001	1000000
Left Shift 7	0001	0010	0011	0000000
BCD	1	2	3	0000000

Table 2.2: Double dabble algorithm used to convert the binary representation of 123 into its BCD representation.

2.10 Detecting Heart Rate

In order to measure heart rate using any sort of sensor, some basic limiting parameters need to be established. A normal healthy heart rate is around 40 bpm to 180 bpm, so by choosing a range from 1 bpm to 300 bpm, all possible human heart rates are covered. This equates to a heart rate frequency span from approximately 0.017 Hz to 5 Hz. The "ventricular systole" is the phase of the heart's cardiac cycle when blood is pumped out from the heart and into the body, this phase lasts approximately 270 ms and the arteries are under pressure (expanded) for roughly 200 ms. The entire cardiac cycle lasts around 800 ms (this time is of course subject to the heart rate at the moment) [35]. Therefore, a pulse wave from the heart that expands the blood vessels lasts around 25% of the entire cardiac cycle. By overcompensating and assuming a heart rate of 5 Hz, the pulse wave is estimated to last only 50 ms. This means that a sensor would need to detect whatever changes induced by the pulse wave at least once every 50 ms in order to detect an abnormally high heart rate. Or in other words, the sensor needs a sampling frequency of 20 samples per second.

Chapter 3
Methodology

This chapter presents the methodology which consists of two major parts, the simulation of the circuit and the physical measurements of the circuit. The reader and sensor system for readout of resistive strain in a stretchable sensor can be seen in Figure 3.1.

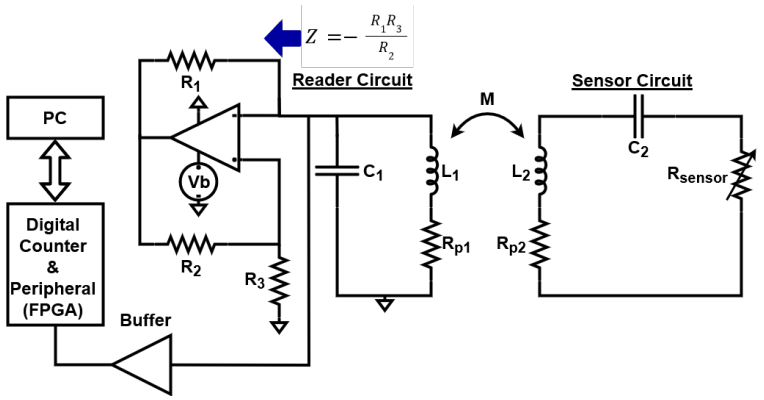

Figure 3.1: Developed wireless readout system for a stretchable strain sensor.

3.1 Simulation

The two possible circuit topologies for the reader and sensor system in this project were the PS and PP topology. Both topologies were simulated to see how parameter variations (resistance, inductance and capacitance) as well as variations in coupling factor affects the oscillation frequency in the coupled system. The variation in coupling factor from 0.6 to 0.4 acts as a substitute for a separation distance of ca 0 mm to 5 mm as shown in Figure 2.7.

The simulated PS and PP circuits can be seen in Figure 3.2 and 3.3, where R_1, R_2 and R_3 belongs to the NIC and is explained in section 2.8, C_1, L_1 and R_{p1} is the reader LC resonator and C_2, L_2, R_{p2} and R_{sensor} makes up the sensor RLC resonator. The first simulations were performed to get a broader understanding of

how the system would behave when subjected to parameter variations. Therefore the T-equivalent circuit presented in section 2.4 wasn't used and coupling was instead achieved by using LTspices "SPICE directive" for inductive coupling [36]. The parasitic capacitance from section 2.6.1 wasn't included either.

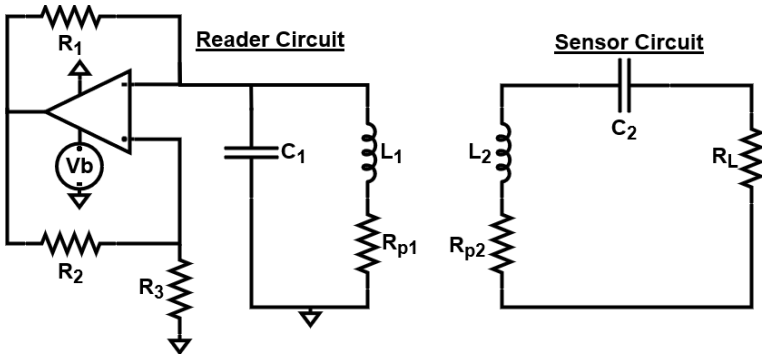

Figure 3.2: PS circuit topology used in the LTspice simulations.

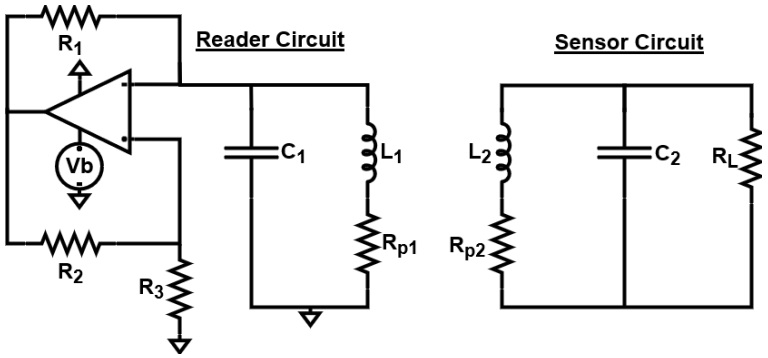

Figure 3.3: PP circuit topology used in the LTspice simulations.

The RLC components were varied as follows: R_{sensor} was varied from 10 Ω to 75 Ω, L_2 was varied from 880 nH to 1270 nH and C_2 was varied from 0.01 nF to 2 nF. The range of the parameters were chosen to correspond to the potential initial values for a stretchable circuit, as well as the potential change in resistance, inductance and capacitance that can occur when such a circuit experiences strain. Since the resistance and capacitance are easier to control when fabricating stretchable sensors, i.e, changing the physical size or material of R_{sensor} or the size of C_2 as opposed to changing the design of L_2, these parameters have relatively larger percentage variation compared to the inductor. Having a greater range of simulated values allows for a better understanding of how variations in the different components affect the readout signal and can therefore be used to find the optimal sensor parameters for a desired effect, such as higher sensitivity to resistance variations. Information form the manufactures of the stretchable electronics indicated that and that the sensor capacitance (C_2) would be difficult to make larger than

a few nF, this limitation is reflected in the chosen C_2 interval.

The sensor components that weren't varied during simulation were kept at the following constant values, $R_{sensor} = 10\ \Omega$, $C_2 = 1$ nH and $L_2 = 880$ nH. C_1 was given the value 1 nF and 10 nF during the simulations to see how it would affect the signal behaviour and L_1 was given the value 980.5 nH since this was the measured value of the square FPC coil from section 2.6.

The goal of this system is to make it sensitive to parameter variations for a certain component, the chosen component is the sensor resistance (R_{sensor}). This means that when analyzing the simulation results, the desired operational parameters should ideally suppress the sensitivity to variations in sensor inductance and capacitance while enhancing the sensitivity to variations in sensor resistance. Figure 3.4, 3.5 and 3.6 shows the LTspice simulations. These figures were further analyzed for specific parameter intervals to find the aforementioned desired operational parameters.

The following parameter intervals for R_{sensor}, C_2 and L_2 were chosen as they showed the desired behavior of having a higher sensitivity to R_{sensor} variations and a lower sensitivity to C_2 and L_2. For R_{sensor}, 10 Ω to 20 Ω, an increase in resistance of 100%. For C_2, 1 nF to 2 nF, an increase of 100%. For L_2, 880 nH to 1,060 nH, an increase of ca 20%. The frequency shifts were first modified to show the sensitivity to percentage change in resistance, capacitance and inductance variations. The sensitivity was then further modified by taking into account the effect strain has on the component values using the information from section 2.3.1. The sensitivity is shown in Figure 3.7 and is presented as Hz per percentage increase in strain. For example, the second bar from the left in the PS Topology graph means that at $C_1 = 1$ nF the frequency will increase by approximately 8000 Hz for every 1% of strain that R_{sensor} experiences.

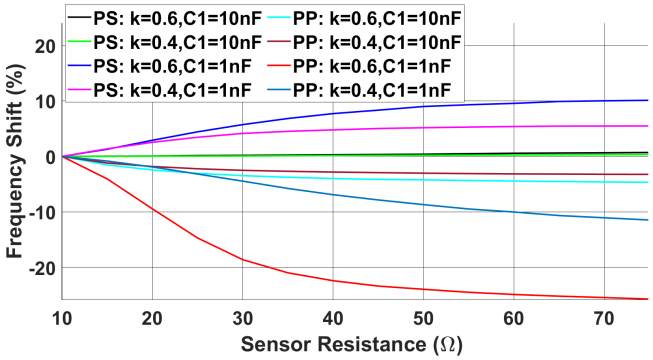

Figure 3.4: LTspice simulation of frequency behaviour caused by variations in sensor inductance (R_{sensor}).

Figure 3.7 shows that the chosen parameter ranges do indeed suppress the sensitivity to variations in sensor capacitance and inductance while greatly increasing the sensitivity to variations in sensor resistance.

After finding appropriate component intervals, more accurate simulations were performed. In the next simulations, both the T-equivalent circuit described in

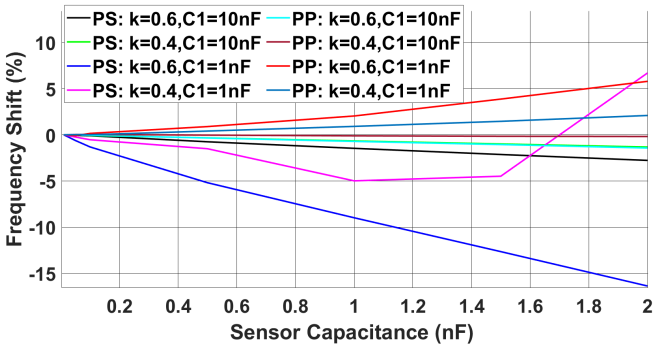

Figure 3.5: LTspice simulation of frequency behaviour caused by variations in sensor capacitance (C_2).

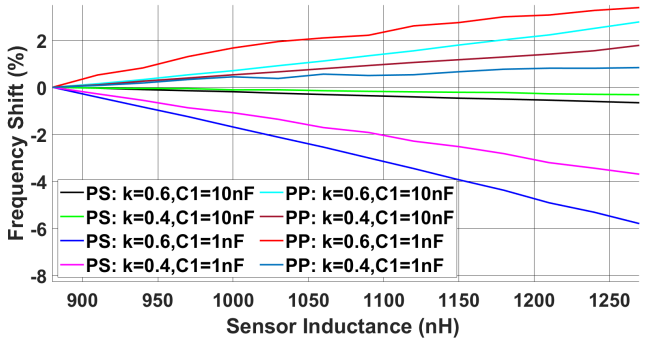

Figure 3.6: LTspice simulation of frequency behaviour caused by variations in sensor inductance (L_2).

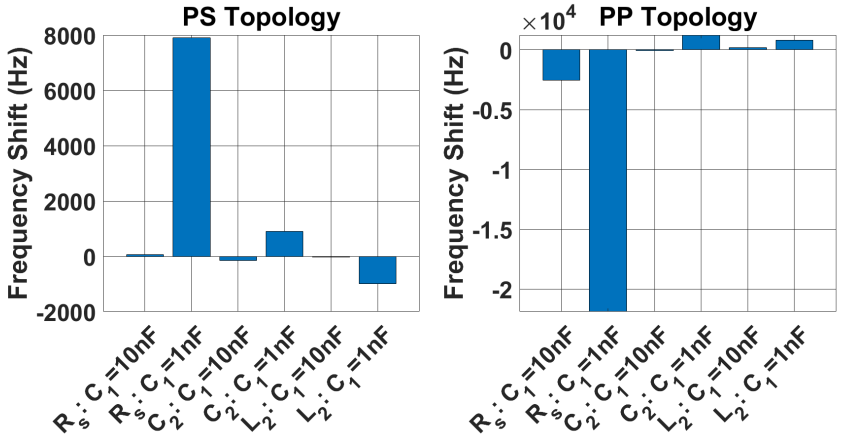

Figure 3.7: Sensitivity comparison between the PS and PP topology according to LTspice simulations.

section 2.4 and the parasitic capacitance explained in section 2.6.1 were taken into consideration. The parasitic capacitance value chosen was for an air insulator at ca 1 mm separation distance, approximately 14 pF. The new simulated circuits can be seen in Figure 3.8 and 3.9 where C_p is the parasitic capacitance between the planar coils and M is the mutual inductance between the planar coils.

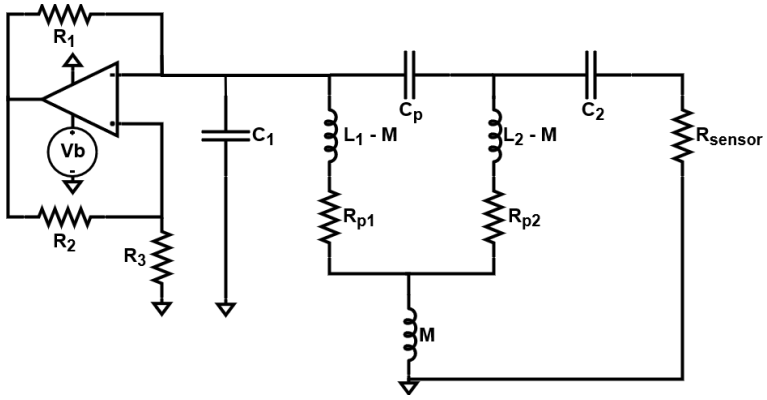

Figure 3.8: PS topology circuit simulated in LTspice when using the T-equivalent circuit and accounting for parasitic capacitance.

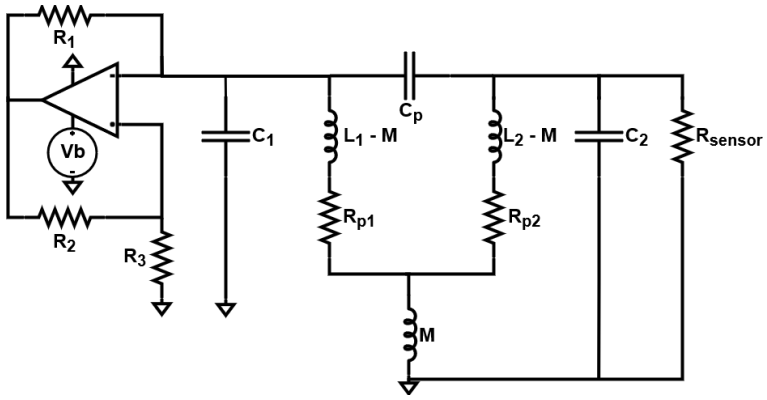

Figure 3.9: PP topology circuit simulated in LTspice when using the T-equivalent circuit and accounting for parasitic capacitance.

These simulations were performed after the first prototype of the stretchable sensor had been constructed, hence more accurate knowledge was known regarding what parameter values that are possible to manufacture. The prototype seen in Figure 2.12 consists of a stretchable planar coil and sensor resistance. The planar coil had an initial inductance of 881 nH and internal resistance (R_{p2}) of 3.6 Ω. The initial sensor resistance was 12.2 Ω The planar coil was stretched up to 25% and the inductance was measured using an the same LCR meter (HIOKI 3532-50 LCR HiTESTER) as before. At 25% strain the inductance had increased to 935 nH, an

increase of ca 6.1% and the internal resistance remained unchanged. The strain measurements are presented in Figure 3.10. Because of the prototype the chosen

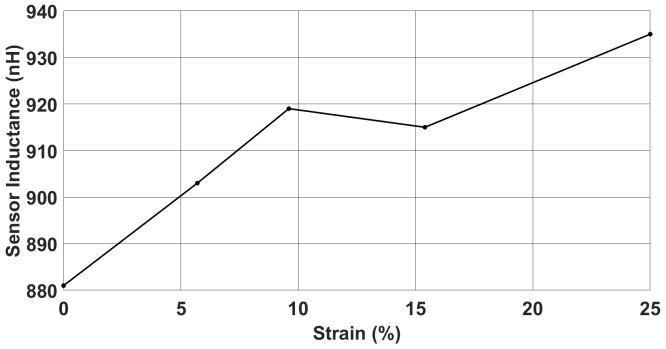

Figure 3.10: Inductance increase with strain on prototype stretchable sensor.

sensor inductance (L_2) range simulated was 880 nH to 940 nH. Additionally, when the planar coil is stretched up to 25%, only 80% of the sensor coil overlaps with the reader coil. At the small separation distances used in this project (single digit mm) it is assumed that this reduction in overlap directly and proportionally affects both the coupling factor and the parasitic capacitance between the reader and sensor coils. The simulation therefore reflects a linear reduction of both the coupling factor and parasitic capacitance up to a total of 20% at 25% strain. Further discussions with the manufacturers of the stretchable electronics revealed that the sensor resistance (R_{sensor}) can reasonably be made as small as 5 Ω. The following parameter ranges were therefore chosen, for R_{sensor}, 5 Ω to 40 Ω. C_2 was given a value from 1.4 nH to 2 nH which is the same interval used for the sensitivity analysis in Figure 3.7. The R_{sensor} interval gives more information over a larger area of values and the C_2 interval eliminates unnecessary component values that would not be feasible or difficult to manufacture. The components that weren't varied during simulation were this time kept at the following constant values, $R_{sensor} = 5$ Ω, $C_2 = 1.4$ nH and $L_2 = 880$ nH. The simulations were performed with a coupling constant of 0.4 to 0.9. The average frequency shift for each component can be seen in Figure 3.11, 3.12 and 3.13 and the simulations for each separate coupling factor value can be found in the appendix. As with the first set of simulations, the sensitivity for the different circuit topologies and reader capacitance value are presented in Figure 3.14. The component ranges chosen for the new sensitivity summary is slightly different from the first simulation. For R_{sensor}, 5 Ω to 20 Ω, for C_2, 1.4 nF to 2 nF and for L_2, 880 nH to 940 nH.

3.2 Coupled Mode Theory Simulations

The PS and PP topologies were simulated using CMT presented in section 2.2. The different RLC components (resistance, inductance and capacitance) were varied and the sensitivity was analyzed. The simulations are presented in Figure 3.15 to

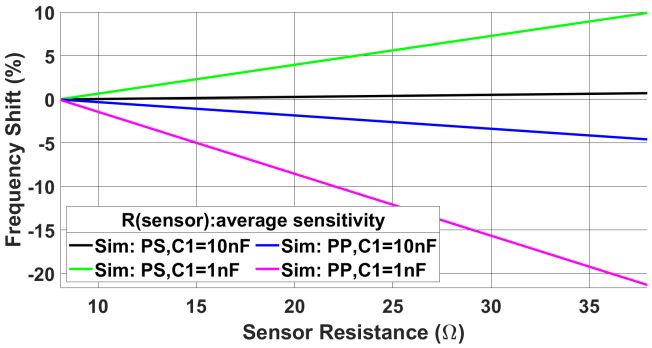

Figure 3.11: LTspice simulation of sensor resistance variations with prototype data.

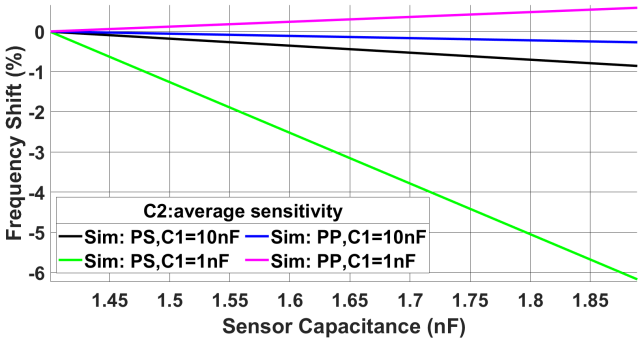

Figure 3.12: LTspice simulation of sensor capacitance variations with prototype data.

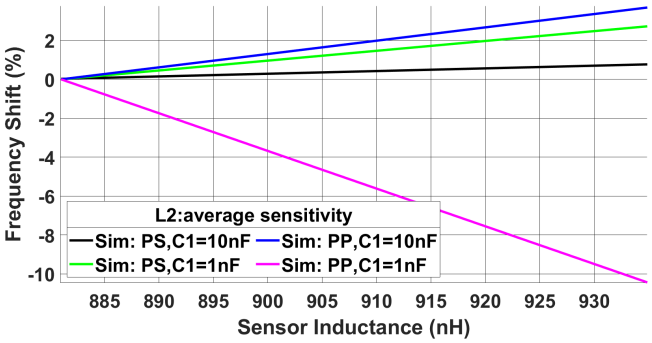

Figure 3.13: LTspice simulation of sensor inductance variations with prototype data.

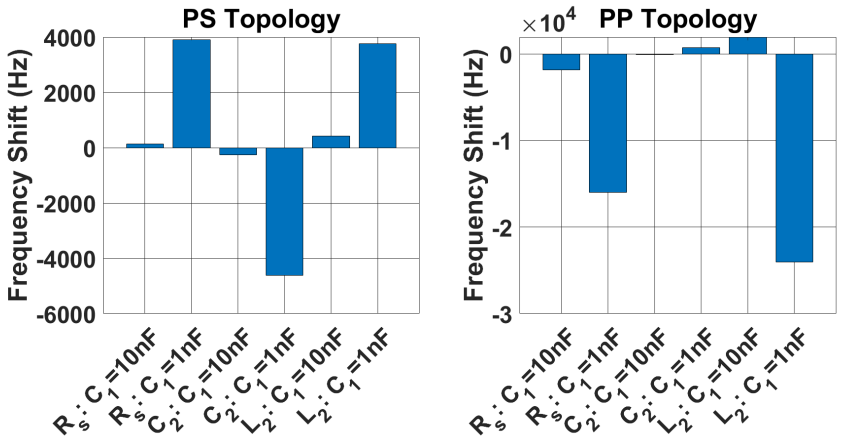

Figure 3.14: Sensitivity comparison between the PS and PP topology with more accurate LTspice models.

3.20. For the PP topology, the sensitivity towards variations in sensor inductance (Figure 3.16) and sensor capacitance (Figure 3.17) are rather linear for the chosen range of values. The sensitivity is very high for small values of sensor resistance (Figure 3.15) but much lower for higher values. Similar behaviour can be seen for the sensor inductance and capacitance in the PS topology as seen in Figure 3.19 and 3.20. However, the sensitivity towards variations in sensor resistance (Figure 3.18) is relatively linear for the whole range of resistance values.

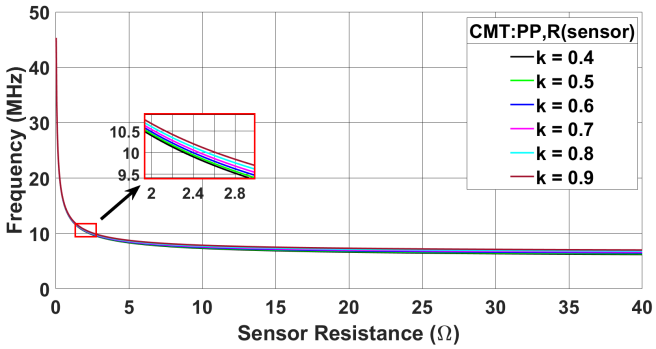

Figure 3.15: Frequency shift caused by variations in sensor resistance of a PP topology circuit according to coupled mode theory.

These simulations indicate that by choosing the PS topology, the choice of possible sensor resistance values would increase which would simplify the manufacturing process of the sensor. The required negative impedance for the NIC can be found by balancing the loss and gain factors from Table 2.1. The negative impedance for both the PS and PP topologies can be seen in Figure 3.21.

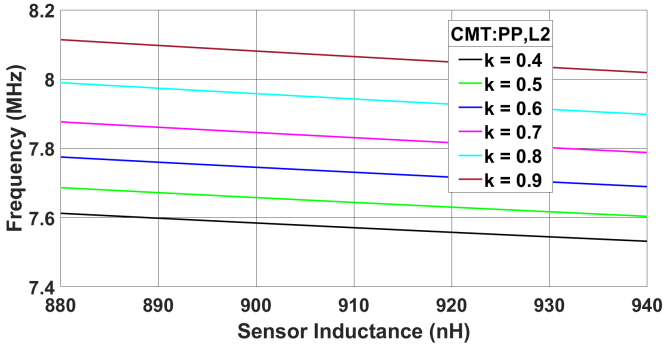

Figure 3.16: Frequency shift caused by variations in sensor inductance of a PP topology circuit according to coupled mode theory.

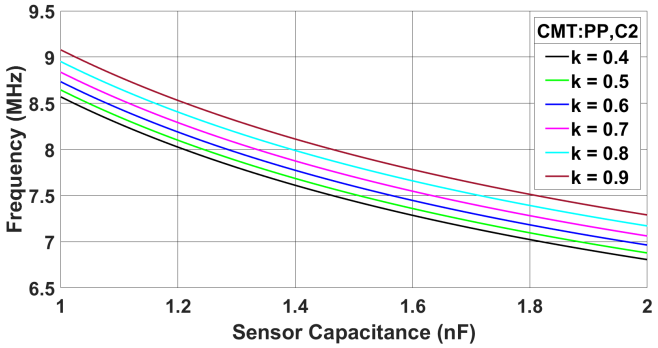

Figure 3.17: Frequency shift caused by variations in sensor capacitance of a PP topology circuit according to coupled mode theory.

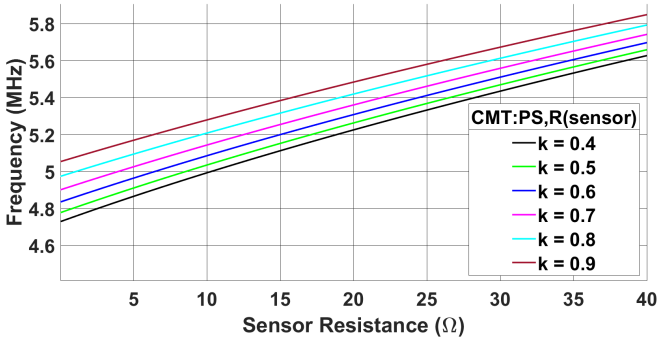

Figure 3.18: Frequency shift caused by variations in sensor resistance of a PS topology circuit according to coupled mode theory.

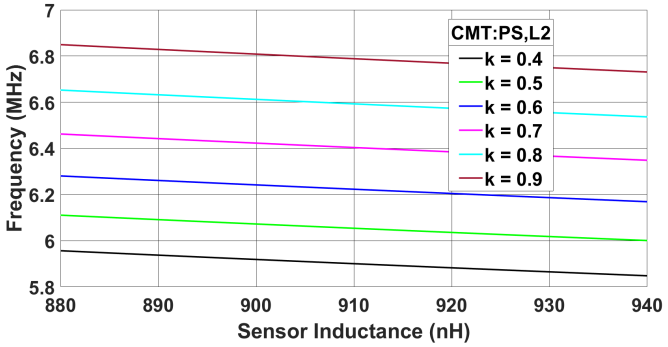

Figure 3.19: Frequency shift caused by variations in sensor inductance of a PS topology circuit according to coupled mode theory.

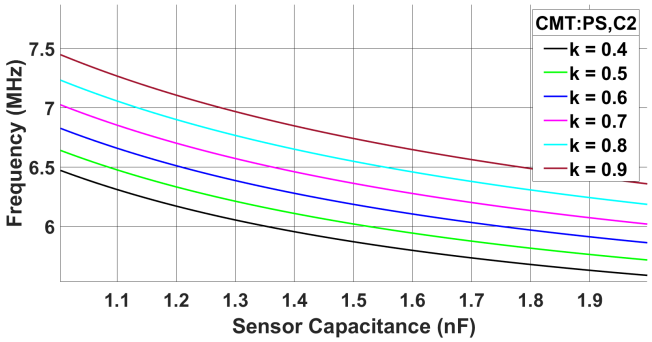

Figure 3.20: Frequency shift caused by variations in sensor capacitance of a PS topology circuit according to coupled mode theory.

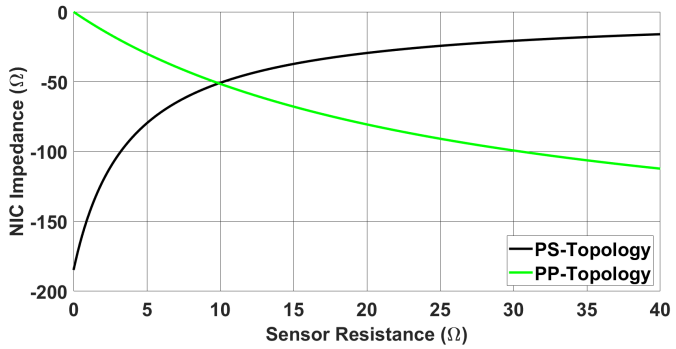

Figure 3.21: Required negative impedance for the PS and PP-Topologies according to coupling mode theory.

3.3 Reader Circuit

In order to perform physical measurements and evaluate the system, a reader circuit is needed. The circuit, as has been stated before, was first simulated with the software LTspice. It was then designed in Kicad and a PCB was printed via PCBgogo. The reader consists of an LC resonator and negative impedance converter (NIC). The square flexible FPC coils in Figure 2.11 were used as the inductor in the LC tank. By inductively coupling a RLC resonator to the LC resonator, the system will produce an oscillating sine wave whose frequency is controlled by all the components in the LC and RLC resonator. The negative impedance value chosen for the NIC was -50 Ω since this value works for both the PS and PP topology as seen in Figure 3.21.

The PCB is also designed with connections for an FPGA (Cmod A7-35T[37]). The FPGA is used as a frequency counter that measures the oscillation frequency of the system. It also handles the UART communication with the PC so that the sampled data can be displayed and analyzed more easily. It was observed during testing of the system that the oscillating signal produced in PCB was too weak to be detected by the FPGA. The FPGA's digital I/O pins won't detect a signal if it is too low and the oscillating signal had an amplitude of 825 mV which was too low. A buffer was therefore externally equipped between the oscillating signal and the I/O pin on the FPGA. The buffer amplified the signal to an amplitude of 2.56 V, high enough to be detected by the FPGA. The signal before and after the buffer can be seen in Figure 3.22. As is evident, the buffer saturates the sine wave and turns it into a square wave. This is no problem since the FPGA only detects logical zeros and ones (not the wave form itself) and the oscillation frequency is not changed by the buffer. The ripples seen in the saturated signal doesn't cause any problems either for the measurements since they are too small to be detected by the FPGA.

The PCB was designed with upgrades in mind. It therefore also contains connections for both analog and digital potentiometers that can be used to fine-tune the NIC. It also has connections for a seven segment display that can be used to visualize the measurement results. The entire PCB circuit can be seen in Figure 3.23. Furthermore, it also contains footprints for an ADC and additional Op-amps that were, in the end, not used.

3.4 FPGA

The FPGA state diagram can be seen in Figure 3.24; it cycles between 5 states that perform the sampling, encoding and transmission of the frequency data from the PCB. The 5 states themself consist of 6 side modules that handle different tasks. The first "Reset State" is used to perform any necessary startup calibration that might be needed or other setups that only needs to be performed once.

3.4.1 Clear State

In the "Clear State", signals are sent to all the 6 side modules which inform them that they should reset all the relevant registers. The FPGA remains in the "Clear

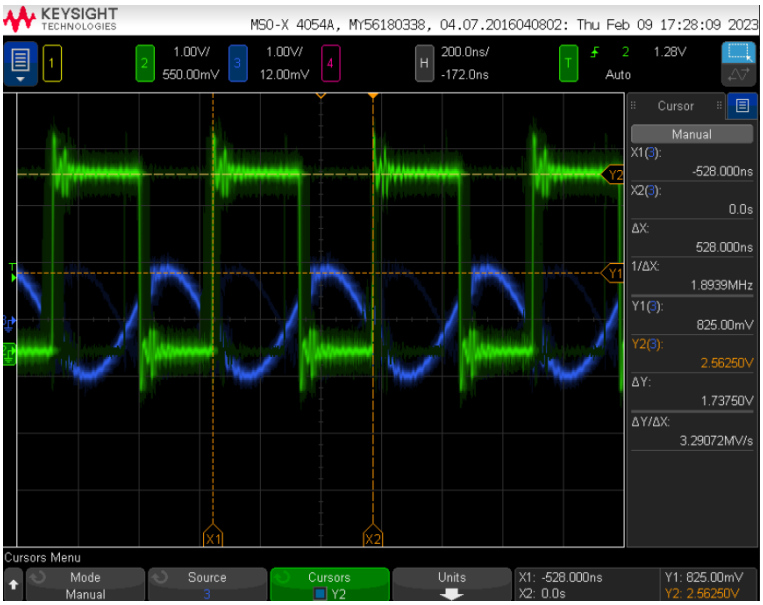

Figure 3.22: Oscillating signal before (blue sine wave) and after (green square wave) the buffer.

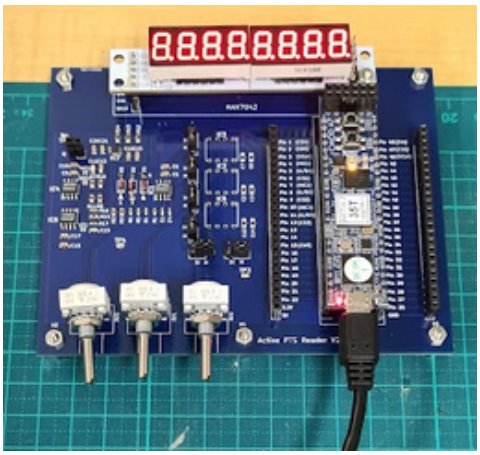

Figure 3.23: PCB used for evaluation of the system.

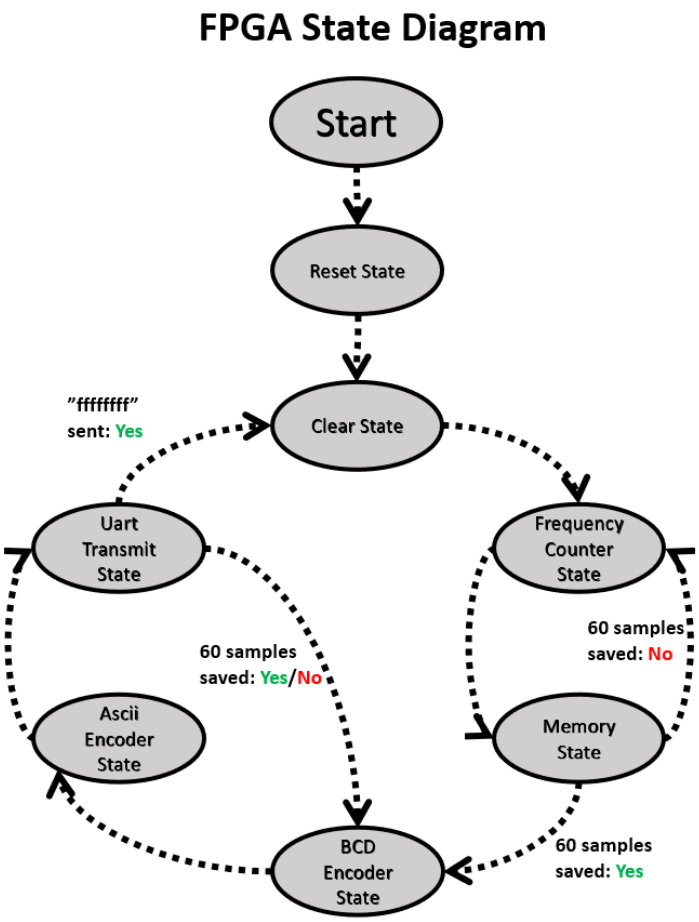

Figure 3.24: FPGA state diagram.

State" for 10 clock cycles before moving to the next state to make sure that the FPGA is given enough time to reset the registers and avoid data corruption.

3.4.2 Frequency Counter/ Memory State

The next state is the "Frequency Counter State", here the FPGA measures the oscillation frequency of the reader. The oscillation frequency in the reader is dimensioned to be around 1.6 MHz (for a reader capacitance of 10 nF) and around 3.4 MHz (for a reader capacitance of 1 nF) which means that the 12 MHz internal clock in the FPGA can be used to implement the frequency counter. The state diagram of the frequency counter is shown in Figure 3.25. Before the frequency counter starts counting, the register for the internal clock ($iclk\_cnt$), the register for the external reader signal ($freq\_cnt$), the register for the current external signal state (new_freq) and the register for the old external signal state (old_freq) are set to 0. For every rising edge of the internal clock, the following tasks are executed using sequential logic. The $iclk\_cnt$ register is incremented, the external signal state ($\_freq$) is registered in the register new_freq. If the current signal state new_freq is not equal to the old signal state old_freq and the new signal state is high (a logical 1) a new rising edge of the external signal has occurred and the frequency counter register $freq\_cnt$ is incremented and the register old_freq is given the current signal state. If the last If-statement is false then there is no new rising edge and the incrementation step is skipped. The $iclk\_cnt$ register is checked to see if the number of iclk pulses has reached a predetermined limit. Several different limits were tested and the chosen one was 200,000 clock pulses from the 12 MHz internal clock which is equal to ca 16.67 ms. If the limit isn't reached, the counting continues. If the limit is reached, the resulting counted frequency is sent from the frequency counter module to the memory and the registers are again reset to 0.

A frequency counter implemented in this manner can theoretically at most be used to count a frequency from $1/16.67$ ms $\approx$ 60 Hz up to 6 MHz (limit set by the Nyquist Theorem). The implementation and FPGA is however not infallible and the current version was tested and proved to be accurate in the frequency span from 100 Hz to ca 5 MHz as can be seen in Figure 3.26 where a signal was generated by a waveform generator and sampled by the FPGA. The largest deviation from the generated signal was 49 Hz, this accuracy is enough for this project.

The transmission of the frequency data between the FPGA and PC was the most time consuming process in the system. This limits the amount of samples that can be displayed without lag in the PC. For this reason, a larger set of samples were recorded and saved in the FPGA memory before transmitting them to the PC. In the current system the FPGA records 60 samples over 1 second before moving to the next state. One sample consists of 17 bits meaning that all the frequency samples are stored in "one" 1020 bit register.

When all the frequency samples are acquired, they are encoded in a format that is convenient to transmit, receive and easy to understand for humans. The ascii format is easy to understand and many programming languages like python already have predefined functions for handling ascii. Before encoding the frequency sample into ascii they are encoded in a binary coded decimal (BCD) format.

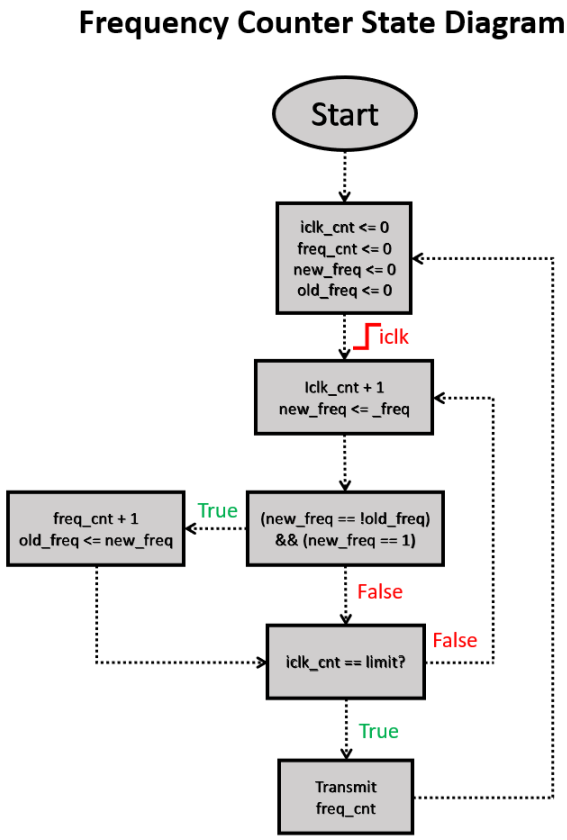

Figure 3.25: State diagram of the FPGA implemented frequency counter.

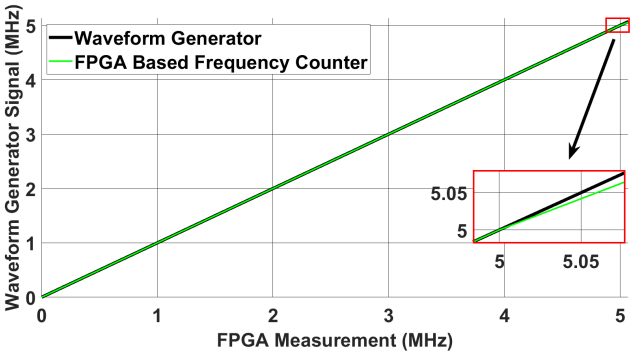

Figure 3.26: Accuracy of the FPGA implemented frequency counter.

3.4.3 BCD Encoder/ ASCII Encoder/ UART Transmit States

Lastly the FPGA cycles between the final three states where one frequency sample is handled at a time. In the “BCD Encoder State” the frequency data is encoded in a BCD format as explained in the section 2.9. The BCD encoded sample is stored in a 32 bit register which is sent to the “ASCII Encoder State”. Here the sample is encoded in the ascii format and stored in a 80 bit register. Finally the frequency sample is transmitted to the PC in the “UART Transmit State. As the name suggests, the data is transmitted from the FPGA to the user via universal asynchronous receiver-transmitter (UART) communication. The baud rate used is 9600 bits/s, the start bit is a 0 and the stop bit is a 1. The FPGA sends 8-bits (one ascii symbol) per transmission along with the start and stop bit. When all the frequency samples are transmitted, one last transmission of “ffffffff” is sent to notify the PC that the transmission is completed and the FPGA enters the "Clear State".

3.5 Measurement Setup

Two different sets of strain measurements were prepared for testing R_{sensor} and C_2 , systematic strain and active strain. Both types of measurements were ideally to be performed when using the reader capacitance (C_1) of value 1 nF and 10 nF, however not all the measurements were possible to perform because the sensors broke before all the measurements could be performed. In the systematic strain measurement the sensor is stretched mechanically using a vise and in the active strain measurement the sensor is stretched manually by hand.

By placing the different sensor components (resistor or capacitor) on the vise, strain can be separately focused on each component. The amount of strain that can be placed on each component is decided by, among other things, the material and architecture. I.e, not every component can be stretched the same amount. In order to determine the strain sensitivity as well as the behavior, robustness and recovery capability of R_{sensor}, it is stretched and relaxed up to 50% in 10% increments. The same type of strain test is performed with C_2 which is stretched up to 35% in 5% increments.The setup used can be seen in Figure 3.27.

During the active strain measurements, R_{sensor} and C_2 are not stretched specific amounts since this would be very difficult to do with accuracy. The components are instead stretched with several levels of increasing strain and later relaxed.

When performing strain on L_2 the vise was not used. This is because the vise is made out of metal and if placed directly underneath the reader and sensor coil, would inevitably affect the inductive coupling. L_2 was instead stretched up to 25% and fixed on a glass substrate using tape.

A pulse wave detection test was also prepared where the sensor is placed on a person’s wrist as seen in Figure 3.30. When the heart sends out a pulse wave, the artery in the wrist expands, this in turn deforms the sensor resistance. A photoplethysmography (PPG) sensor was used as a reference heart rate measurement.

From the LTspice simulations in section 3.1 the fully stretchable RLC sensors in Figure 3.28, 3.29 and 3.30 were constructed. These sensors were used to perform

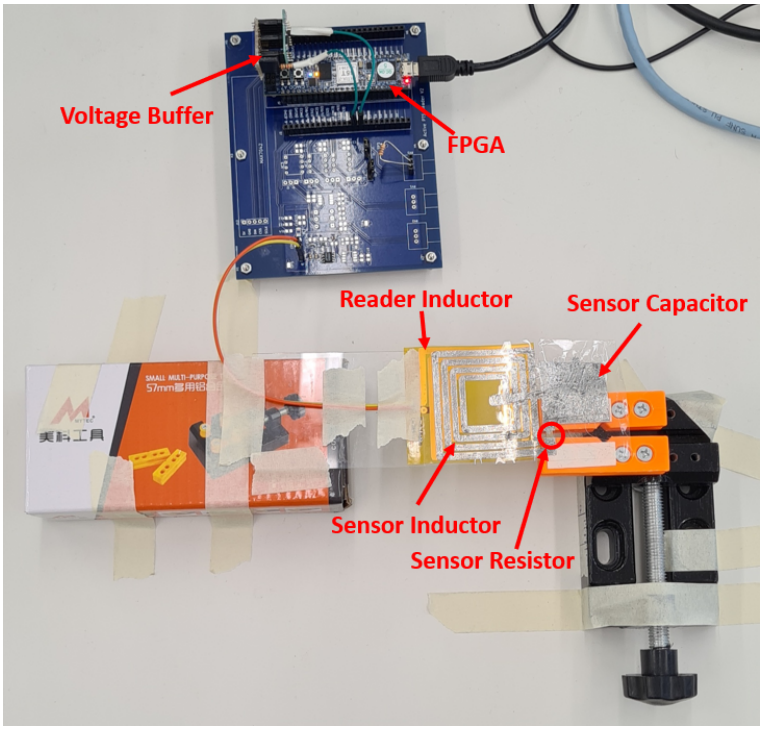

Figure 3.27: Measurement setup for systematic resistive strain.

strain measurements by coupling the stretchable sensor to the reader circuit by placing the coils in close proximity as seen in Figure 3.27.

A stable oscillation frequency when parameters are unchanging is of importance when intending to detect frequency shift. Factors such as component temperature and supply voltage could potentially affect the signal stability. To test the significance of the temperature in the circuit, a multimeter with a built-in digital thermometer was used by placing the measurement probe on various points on the PCB and simultaneously measuring the temperature and frequency. Between the different measurements, the PCB was disconnected from the power source and was cooldown for 20 min. The probe was placed on the opamp of the NIC, the opamp of the buffer, C_1 in the LC tank, the PCB board itself, the 35T chip in the FPGA, the USB connection and finally the FPC.

To test the effect of the supply voltage, an external power supply was connected and the supply voltage was varied from 2.4 V to 5.0 V with 0.1 V increments while measuring the oscillation frequency. Lastly, two frequency measurements at a supply voltage of 3.3 V (the supply voltage of the FPGA) were compared to see the difference in signal stability when powering the oscillator via an FPGA or an external power supply.

Figure 3.28: Stretchable parallel RLC sensor, $R_{sensor} = 2\ \Omega$, $L_2 = 881$ nH and $C_2 = 1.4$ nF.

Figure 3.29: Stretchable series RLC sensor, $R_{sensor} = 5\ \Omega$, $L_2 = 881$ nH and $C_2 = 1.4$ nF.

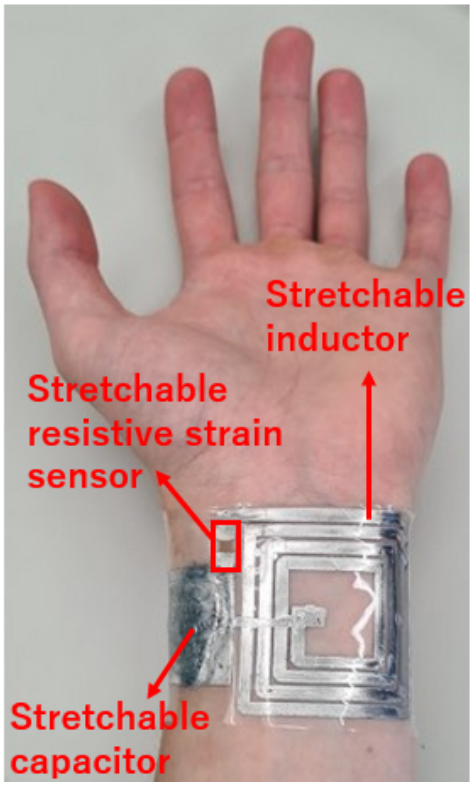

Figure 3.30: Stretchable series RLC sensor placed on wrist for pulse wave detection.

Chapter 4
Results

In this section the results from the experimental strain measurement on the stretchable RLC sensors, the pulse wave detection test and signal stability test are presented. For the two types of strain measurements (systematic and active), only two examples are shown, the rest are allocated to the Appendix.

4.1 Strain Measurement

The strain measurements when stretching the sensor resistance (R_{sensor}) is presented in Figure 4.1 and 4.2. In these measurement examples the reader capacitor (C_1) had a value of 10 nF and the stretchable series RLC sensor in Figure 3.29 was used to form the PS circuit topology.

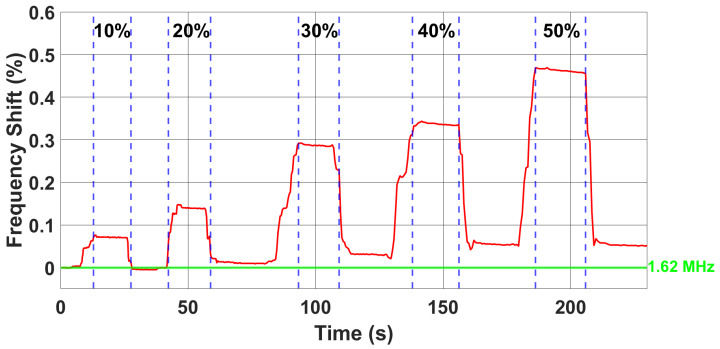

Figure 4.1: Systematically induced strain on R_{sensor} with the PS topology C_1 = 10 nF.

Next, the sensitivity and behavior from all the measurements are extracted from the strain measurements, summarized and compared to the simulations. Figure 4.3 shows the sensitivity towards parameter variations for the simulations compared to the measurements, the graph shows the frequency shift in % caused by 1% of strain in the various RLC components. The frequency behavior comparisons are presented in Figure 4.4, 4.5 and 4.6.

Lastly in Figure 4.7 the pulse wave detection test can be seen.

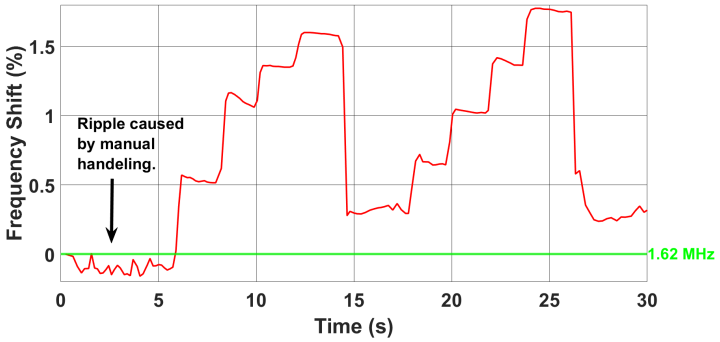

Figure 4.2: Actively induced strain on R_{sensor} with the PS topology $C_1 = 10$ nF.

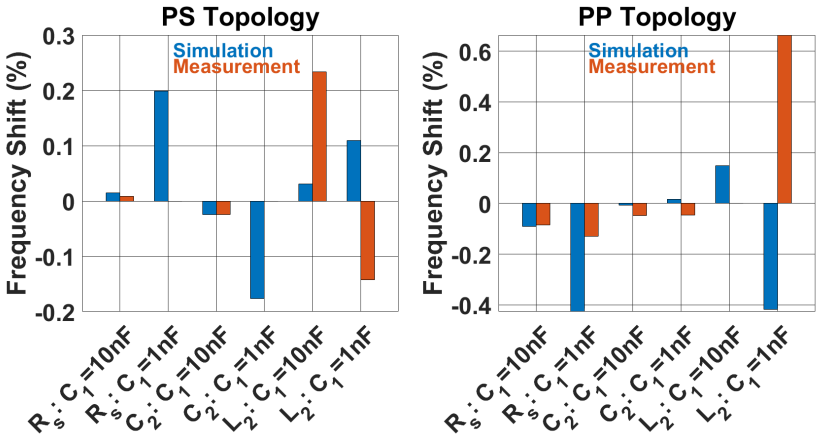

Figure 4.3: Parameter variation sensitivity comparison between simulations and measurements.

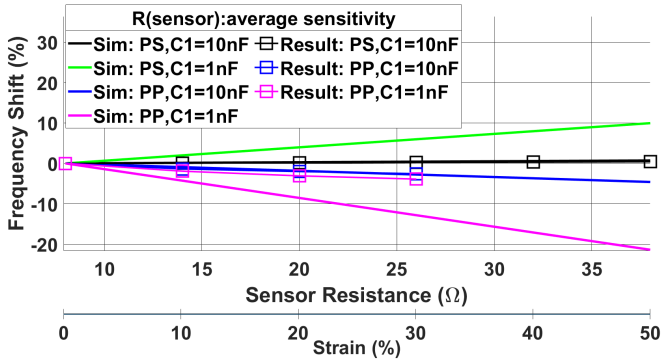

Figure 4.4: Frequency behaviour caused by variations in R_{sensor}.

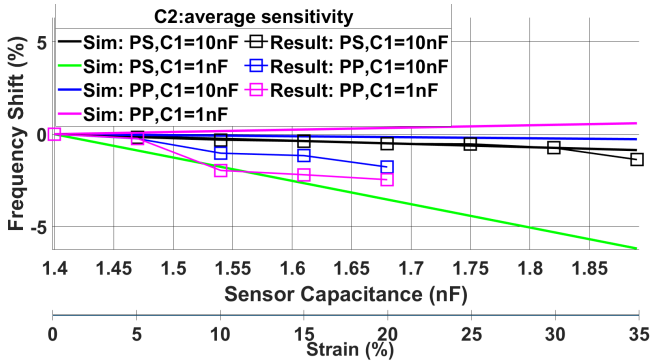

Figure 4.5: Frequency behaviour caused by variations in C_2.

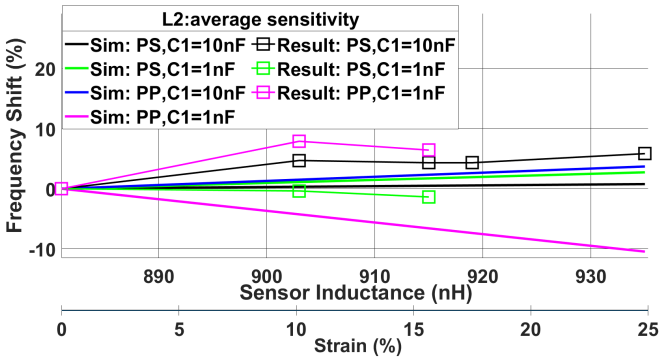

Figure 4.6: Frequency behaviour caused by variations in L_2.

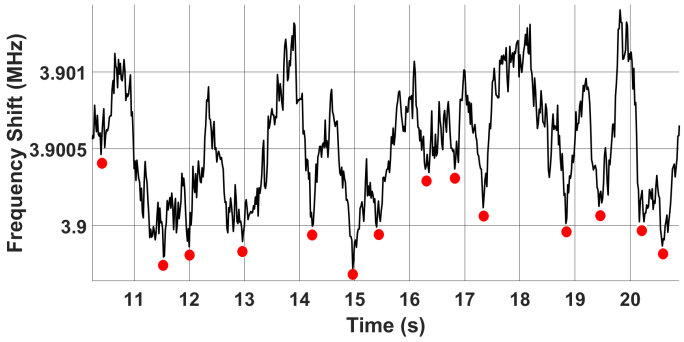

Figure 4.7: Pulse wave detection test using a parallel RLC circuit with a reader capacitor of 1 nF.

4.1.1 Results (Restistive Strain)

By analyzing Figure 4.3 and 4.4 one can see contradictory results regarding the system behavior estimation method. On one hand, the simulation and measurement for both the PS and PP topology when using $C_1 = 10$ nF agrees quite well. On the other hand however, when looking at the measurement for the PP topology with $C_1 = 1$ nF, both the sensitivity and behavior deviates significantly from the simulations. The highest sensitivity measured was with the PP topology and $C_1 = 1$ nF which was -0.129% frequency shift per 1% increase in strain.

4.1.2 Results (Capacitive Strain)

The strain measurements on C_2 in Figure 4.3 and 4.5 only agrees with the simulation in the case of the PS topology with $C_1 = 10$ nF. For this singular case, the sensitivity and behavior up to 30% strain follows the simulations accurately. In the remaining cases, both the sensitivity and behaviour deviates.

4.1.3 Results (Inductive Strain)

In the experiment with strain on the sensor inductance (L_2), one can see from Figure 4.3 and 4.6 that the measurement and simulation deviates for both the sensitivity and behavior regardless of the circuit topology or the value of C_1.

4.1.4 Results (Pulse Wave Detection)

When detecting pulse waves the system setup resulting in Figure A.15 and A.16 was used. Meaning that the when the sensor experiences strain, the oscillation frequency decreases. By counting the dips in Figure 4.7 and taking the average over 60s, a heart rate of 66 bpm could be calculated. The PPG reference sensor showed an average heart rate of 68 bpm during the same time interval.

4.2 Signal Stability Measurements

The temperature measurements showed continuous fluctuations of at most $0.5°C$ on the different components. The measurements with external power supply as well as the comparison can be seen in Figure 4.8 and 4.9.

4.2.1 Results (Stability)

Figure 4.8 shows that the oscillation frequency is dependent on the supply voltage and small variations would indeed affect the signal stability and cause frequency shifts in the order of 0.1%. However, from this figure, smaller variations at constant supply voltages can also be seen. These variations could likely be caused by the fluctuating temperature in the circuit component. Furthermore, in Figure 4.9, one can see the significance of a stable supply voltage. When the oscillator was powered by the external source, the frequency fluctuated with 0.07% and when the FPGA was used, the fluctuation was 0.18%, more than twice as high.

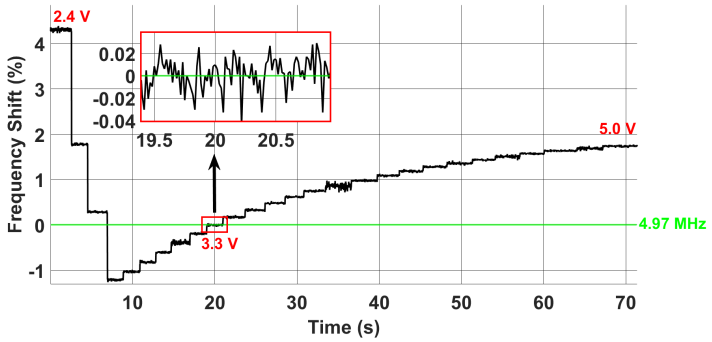

Figure 4.8: Frequency behaviour caused by variations in supply voltage.

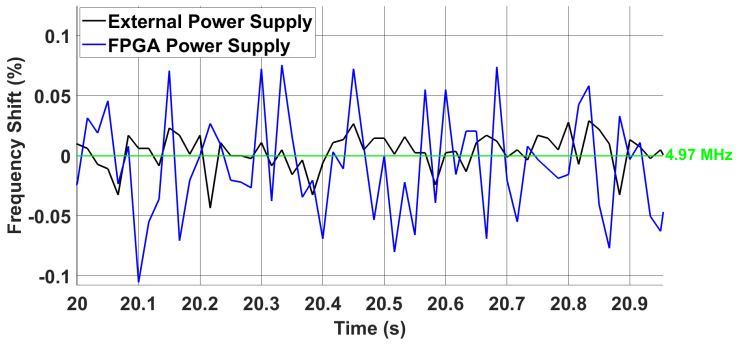

Figure 4.9: Frequency stability comparison when using an external power supply or the FPGA to power the oscillator.

Chapter 5

Conclusion and Discussion

5.1 Concluding Results

All the measurements of L_2 deviates from the simulations and is likely caused by the difficulties of estimating the behaviour of a planar inductor coil when it is stretched. When the coil is stretched it affects multiple parameters. Apart from the self inductance that varies, the overlapping area between the reader and sensor coil will change which means that both the coupling factor and the parasitic capacitance between the two coils will change. This makes the inductance a more difficult parameter to estimate than the resistance or capacitance. Furthermore, in the experiments with R_{sensor} and C_2, when C_1 was given a value of 10 nF the measurements and simulations agreed in 3 out of 4 cases but for the instances when $C_1 = 1$ nF, the measurements deviated significantly from the simulations. This might be explained by the higher reader capacitance. If C_1 is smaller, any parasitic capacitance that might occur between the inductor coils or other components will have a larger effect on the oscillation frequency. If these parasitics are not accounted for correctly during the simulations, then the measurements and simulations will inevitably deviate.

From all the systematic and active strain measurements, a few things can be noted. The system does indeed show varying sensitivity towards strain in the different components as well as towards different circuit topologies and reader capacitance. The reader circuit is fully capable of detecting and distinguishing between various amounts of strain as can be seen in Figure 4.1, A.13, A.15,A.17,A.19 and A.21. And lastly, the stretchable sensors themselves show a relatively good frequency recovery capability when the sensor transitions from a strained to a relaxed state as is prevalent in both the systematic (Figure 4.1, A.13, A.15,A.17,A.19 and A.21) and active (Figure 4.2, A.14, A.16,A.18 and A.20) strain measurements.

From section 4.1.4 one can see that the system was successful in detecting the relatively faint skin deformation caused by the heartbeat of a human via resistive strain when using the PP topology and $C_1 = 1$ nF. It was also capable of detecting the pulse waves over an extended period of time so that the heart rate could be calculated.

5.2 Circuit Evaluation

This project provides a compact and easy to manufacture readout circuit and method. The readout circuit itself consists of a negative impedance convertor (NIC), an LC tank, a buffer and an FPGA. The NIC and LC tank is coupled to the stretchable RLC sensor to generate an oscillating signal whose frequency is determined by the components in the reader and RLC sensor. This makes it possible to detect strain in whichever component the user desires. The oscillator in the project did however experience a fair amount of noise that would undoubtedly affect the result. Via testing it was determined that the noise is likely caused by temperature variations in the circuit components as well as an unstable voltage supply.

5.3 Result Evaluation

A method for analyzing and modeling the behavior and sensitivity of a fully stretchable circuit is of great benefit for the future design and construction with these kinds of electronics. This project investigated the feasibility and accuracy of designing an inductively coupled RLC reader and sensor system where different components have the capability to change. The circuit was first simulated while varying the RLC components (resistance, inductance and capacitance) in the sensor according to a determined parameter range. The parameter range was partly based on previously established research regarding how the components intrinsic value varies when experiencing strain, and partly based on our own tests performed with prototype sensors. The simulations were then used to choose the optimal operational parameters for the desired system behaviour. The simulation method worked to various degrees. The system has room for improvement for the estimation of frequency behaviour when exposing sensor inductance to strain or when the reader capacitance was given a low value. However, when estimating the frequency behaviour of the system for variations in sensor resistance and capacitance while using a higher valued reader capacitance it showed promising results. Furthermore, the system is undoubtedly capable of detecting and measuring different degrees of strain using a simple circuit structure and the FPGA based frequency counter. It is also capable of detecting and measureing heart rate.

5.4 Research Comparison

Inorder to evaluate the functionality and significance of this work, it is compared to previously published research as seen in Table 5.1. From this table it is evident that this work presents far from the highest sensitivity or frequency shift vs strain, but, it is not the lowest sensitivity either. However, because of the simplicity of the FPGA based frequency counter it does presents the least resource heavy readout method. Both vector network analyser (VNA) and impedance analyser are advanced, bulky and expensive equipment that are not suitable for wearable sensors.

The FPGA based frequency counter readout method provides a simple and straightforward way of detecting the strain in the sensor via frequency shift. With an error margin of at most 49 Hz when measuring frequencies between 100 Hz and 5 MHz it can detect any frequency shifts in the hundreds of Hz region. This also means that the accuracy of the readout method is mainly based on the implementation of the oscillator itself. In the case where the FFT was used to find the oscillation frequency, it also utilized an ADC to first record the signal waveform which still requires more components then the FPGA based frequency counter. Another thing of note is the centre resonance frequency F_0. In this work, F_0 is lower than the previous research. This is one of the factors that makes the use of the frequency counter possible. The higher F_0 is, the higher internal frequency is required by the frequency counter module, in this work the FPGA used has an interval clock frequency of 12 MHz. I.e, the frequency counter in this project would be too slow to be implemented with the previous works.

Source	**F_0**	**Freq, shift vs strain**	**Sensor circuit**	**Readout method**
Jiseok Kim 2014 [38]	1.613 GHz	−1.11%	LC	VNA
Lingnan Song 2014 [39]	2.947 GHz	+0.307%	Patch antenna	VNA
Kyeong Jae Lee 2018 [40]	13.56 MHz	−0.0543%	L	Impedance Analyzer
Qian Zhang 2023 [41]	13.80 MHz	−0.368%	LCR	FFT and ADC
This work (PS, C1=10nF)	1.620 MHz	+0.00814%	LCR	Freq. counter
This work (PP, C1=1nF)	3.800 MHz	−0.129%	LCR	Freq. counter

Table 5.1: Comparison of different wireless strain readout methods.

5.5 Conclusion

In conclusion, this project presents a reader circuit that is easy to manufacture and to some extent easy to model. The system is capable of detecting and distinguishing between various amount of strain. When using the PP topology with a reader capacitor of 1 nF acchieves a sensitivity of -0.129% frequency shift per 1% of strain. With this sensitivity it was capable of detecting heart rate via frequency shift without the use of any bulky or advanced equipment or readout methods such as VNA or frequency sweeps. By extension, it it reasonable to assume that the sensor would also be able to detect any detecting any physiological phenomena that induced strain on the skin.

This research was submitted to and accepted by the 66th IEEE International Midwest Symposium on Circuits and Systems (MWSCAS)[42].

5.6 Future work

This project was to some extent successful in achieving its desired goal but there is definitely room for improvement. More work should be directed towards evaluating the sensor performance when it is subjected to vertical and horizontal displacement. These kinds of displacements are unavoidable when a sensor and reader is fixed to a moving subject.

Higher sensitivity is a well sought after trait in medical sensors so more research could be directed towards further increasing the sensitivity. This can be achieved by testing different RLC component values. This project focused more on testing different values for sensor resistance and capacitance, future work could also focus on redesigning the planar coil to investigate whether there are better structures.

One last but crucial improvement would be to address the noise that is right now prevalent in the oscillating signal. The noise from temperature variations could possibly be countered by implementing a filtering algorithm. As for the noise caused by the unstable power supply, this could be addressed by connecting a low noise power supply instead of powering the oscillator directly from the FPGA. One thing to keep in mind is that the power supply should be small and portable so as to not lessen the viability of this project as a potential wearable medical sensor.

5.7 Acknowledgement

Special thank you to Matsuhisa-sensei and Hinata-san from Matsuhisa laboratory at the University of Tokyo. Without their hard work and cooperation in manufacturing the stretchable sensors, this project would not have been possible.

References

[1] Hopkins, Donald R., "Disease Eradication", *N Engl J Med*, vol. 368, no. 1, pp. 54-63, Jan. 2013.

[2] M. Rehman, P. Nallagownden and Z. Baharudin, "Efficiency investigation of SS and SP compensation topologies for wireless power transfer", *Int. J. Power Electron. Drive Syst.*, vol. 10, no. 4, pp. 2157, Dec. 2019.

[3] Song, P., Song, J., Zhang, Y., "Stretchable conductor based on carbon nanotube/carbon black silicone rubber nanocomposites with highly mechanical, electrical properties and strain sensitivity", *Composites Part B: Engineering*, vol. 191, pp. 107979, Jun. 2020.

[4] Niu, S. et al., "A wireless body area sensor network based on stretchable passive tags", *Nat Electron*, vol. 2, pp. 361–368, Aug. 2019.

[5] Lin. R and Kim. HJ and Achavananthadith. S and et al., "Wireless battery-free body sensor networks using near-field-enabled clothing", *Nat Commun*, vol. 11, pp. 444, Jan. 2020.

[6] Matsuhisa. N and Niu. S and O'Neill. S,J,K and et al., "High-frequency and intrinsically stretchable polymer diodes", *Nature*, vol. 600, pp. 246-252, Dec. 2021.

[7] G. -S. Ryu et al., "Flexible and Printed PPG Sensors for Estimation of Drowsiness", *IEEE T-ED*, vol. 65, no. 7, pp. 2997-3004, Jul. 2018.

[8] Wang. S and Xu. J and Wang. W and et al., "Skin electronics from scalable fabrication of an intrinsically stretchable transistor array", *Nature*, vol. 555, pp. 83-88, Feb. 2018.

[9] Park. S and Heo. S.W and Lee. W and et al., "Self-powered ultra-flexible electronics via nano-grating-patterned organic photovoltaics", *Nature*, vol. 561, pp. 516-521, Sep. 2018.

[10] F. Peng and W. Wang and H. Liu., "Development of a reflective PPG signal sensor", *International Conference on Biomedical Engineering and Informatics*, vol. 7, pp. 612-616, Oct. 2014.

[11] Garmin., *Fenix 6 Pro Series: Owner's Manual*, [Online]. Available: https://www8.garmin.com/manuals/webhelp/fenix66s6xpro/EN-US/GUID-9C813064-813F-45E8-9F8E-98A2485B1BB1-homepage.html. [Accessed: 2023-02-09]

[12] Rong, Chao and Zhang, Bo and Wei, Zhihao and Wu, Lihao and Shu, Xujian., "A Wireless Power Transfer System for Spinal Cord Stimulation Based on Generalized Parity Time Symmetry Condition", *IEEE Trans. Ind. Appl.*, vol. 58, no. 1, pp. 1330-1339, Jun. 2022.

[13] X, Wenxun. and S, Ruigeng. and Z, Bo. and Q, Dongyuan. and C, Yanfeng. and X, Fan., "Multiple Parameters Estimation Based on Transmitter Side Information in Wireless Power Transfer System", *IEEE Access*, vol. 7, pp. 164835-164843, Nov. 2019.

[14] R. Jegadeesan and Y. -X. Guo, "Topology Selection and Efficiency Improvement of Inductive Power Links", *IEEE Transactions on Antennas and Propagation*, vol. 60, no. 10, pp. 4846-4854, Oct. 2012.

[15] R. Jegadeesan and Y. X. Guo, "A study on the inductive power links for implantable biomedical devices", *2010 IEEE Antennas and Propagation Society International Symposium*, pp. 1-4, Sep. 2010.

[16] Y. -X. Guo, D. Zhu and R. Jegadeesan, "Inductive wireless power transmission for implantable devices", *2011 iWAT*, pp. 445-448, Mar. 2011.

[17] S. Cui, et al., "Study on efficiency of different topologies of magnetic coupled resonant wireless charging system", *2017 IOP Conf. Ser.: Earth Environ. Sci.*, vol. 93, Sep. 2017.

[18] L. Yambem, M. K. Yapici and J. Zou., "A New Wireless Sensor System for Smart Diapers", *IEEE Sensors Journal*, vol. 8, no. 3, pp. 238-239, Mar. 2008.

[19] B. J. Peterson, A. V. Olson and T. J. Kaiser., "A Wireless Sensor Interrogator Design for Passive Resonant Frequency Sensors Using Frequency Modulation Spectroscopy", *IEEE Sensors Journal*, vol. 10, no. 12, pp. 1884-1890, Dec. 2010.

[20] John C. et al., "Wireless, passive, resonant-circuit, inductively coupled, inductive strain sensor", *Sensors and Actuators A: Physical*, vol. 102, pp. 61-66, Dec. 2002.

[21] Huang, Xian and Liu, et al., "Materials and Designs for Wireless Epidermal Sensors of Hydration and Strain", *Advanced Functional Materials*, vol. 24, no. 25, Jul. 2014.

[22] Liu, J., Yi, Y., Zhou, Y. et al., "Highly Stretchable and Flexible Graphene/ITO Hybrid Transparent Electrode", *Nanoscale Res Lett*, vol. 11, no. 108, Feb. 2016.

[23] Park, T.H., Ren, W., Lee, H.J. et al., "Efficient TADF-based blue OLEDs with 100% stretchability using titanium particle-embedded indium zinc oxide mesh electrodes", *NPG Asia Mater*, vol. 14, no. 66, Aug. 2022.

[24] Sim, K. et al., "An epicardial bioelectronic patch made from soft rubbery materials and capable of spatiotemporal mapping of electrophysiological activity", *Nat Electron*, vol. 3, pp. 775–784, Nov. 2020.

[25] Liang, Bo and Wei, Jinwei, et al., "High Resolution Direct Writing Liquid Metal Patterns for Printed Stretchable Electronics", *2018 IEEE SENSORS*, pp. 1-4, Oct. 2018.

[26] *Gallium–Indium eutectic*, [Online]. Available: `https://www.sigmaaldrich.com/JP/en/product/aldrich/495425`. [Accessed: 2023-04-18]

[27] Fernandes, D F., Majidi, C., Tavakoli, M., "Digitally printed stretchable electronics: a review", *J. Mater. Chem. C*, vol. 7, pp. 14035-14068, Sep. 2019.

[28] Matsuhisa, N. et al., "High-Transconductance Stretchable Transistors Achieved by Controlled Gold Microcrack Morphology", *Adv. Electron. Mater.*, vol. 5, pp. 1900347, Jul. 2019.

[29] David K. Cheng., *Field and Wave Electromagnetics*, 2nd Edition, Pearson (2014)

[30] Behzad Razavi., *RF MICROELECTRONICS*, 2nd Edition, Pearson (2012)

[31] *NFC/RFID Planar Spiral Coil Inductance Calculator*, [Online]. Available: `https://www.translatorscafe.com/unit-converter/pt-PT/calculator/planar-coil-inductance/`. [Accessed: 2023-02-03]

[32] HIOKI E.E. CORPORATION., *A3532-50 LCR HiTESTER*, [Online]. Available: `https://assets.tequipment.net/assets/1/26/Documents/Hioki/3532-50e_04.pdf`. [Accessed: 2023-03-24]

[33] C.B. Falconer., *An Explanation of the Double-Dabble Bin-BCD Conversion Algorithm*, [Online]. Available: `http://www.eprg.org/computerphile/doubledabble.pdf`. [Accessed: 2023-02-09]

[34] *Serially Interfaced, 8-Digit LED Display Drivers*, [Online]. Available: `https://pdf1.alldatasheet.com/datasheet-pdf/view/73745/MAXIM/MAX7219.html`. [Accessed: 2023-02-08]

[35] J.G. Betts., *Anatomy & Physiology*, OpenStax College, Rice University (2013) ISBN:9781938168130

[36] *LTspice: Simple Steps for Simulating Transformers*, [Online]. Available: `https://www.analog.com/en/technical-articles/ltspice-basic-steps-for-simulating-transformers.html`. [Accessed: 2023-03-24]

[37] *Artix-7 FPGAs Data Sheet: DC and AC Switching Characteristics*, [Online]. Available: `https://docs.xilinx.com/v/u/en-US/ds181_Artix_7_Data_Sheet`. [Accessed: 2023-02-15]

[38] J. Kim, Z. Wang and W. S. Kim, "Stretchable RFID for Wireless Strain Sensing With Silver Nano Ink," *IEEE Sensors Journal*, vol. 14, no. 12, pp. 4395-4401, Dec. 2014,

[39] Lingnan Song, Amanda C. Myers, Jacob J. Adams, and Yong Zhu., "Stretchable and Reversibly Deformable Radio Frequency Antennas Based on Silver Nanowires", *ACS Applied Materials Interfaces*, vol. 6, pp. 4242-4253, Mar. 2014.

[40] Lee, Kyeong Jae, Namsun Chou, and Sohee Kim., "A Batteryless, Wireless Strain Sensor Using Resonant Frequency Modulation", *Sensors*, vol. 18, no. 11, pp. 3955, Nov. 2018.

[41] Qiang Zhang, Fransiska M. Bossuyt, Naomi C. Adam, et al., "A Stretchable Strain Sensor System for Wireless Measurement of Musculoskeletal Soft Tissue Strains", *Advanced Materials Technologies*, vol. 1, Apr. 2023.

[42] Billy Mårtensson, Hinata Mitomo, Baktash Behmanesh, Naoji Matsuhisa, Hiroki Ishikuro., "An Oscillator with Inductively Coupled Resonators for Readout of Stretchable Resistive Strain Sensor", *MWSCAS*, Aug. 2023.

Appendix A

Simulations and Measurements

A.1 LTspice Simulation

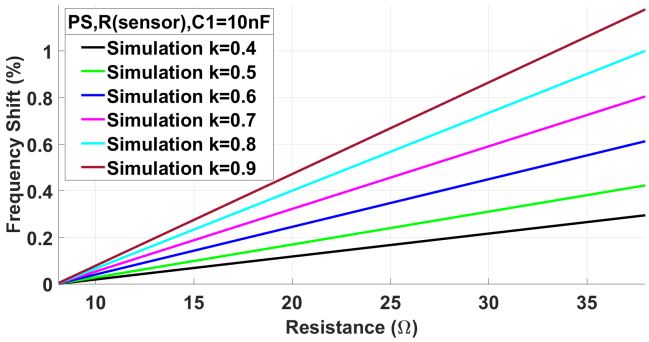

Figure A.1: LTspice simulations for variations in R_{sensor} with the PS topology and $C_1 = 10$ nF.

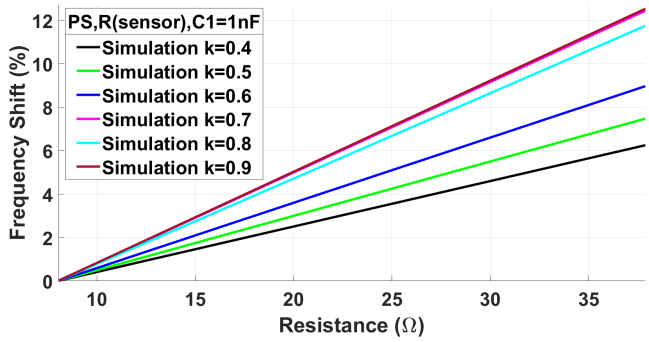

Figure A.2: LTspice simulations for variations in R_{sensor} with the PS topology and $C_1 = 1$ nF.

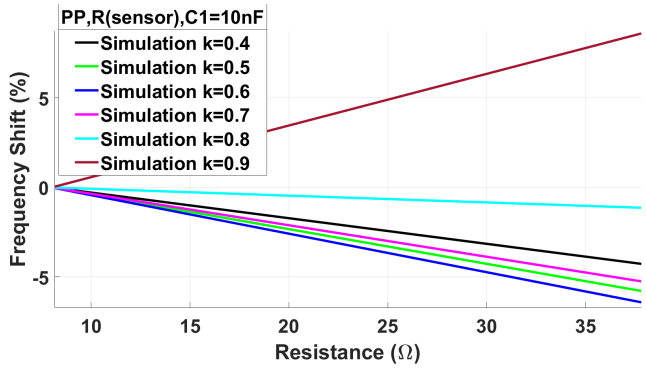

Figure A.3: LTspice simulations for variations in R_{sensor} with the PP topology and $C_1 = 10$ nF.

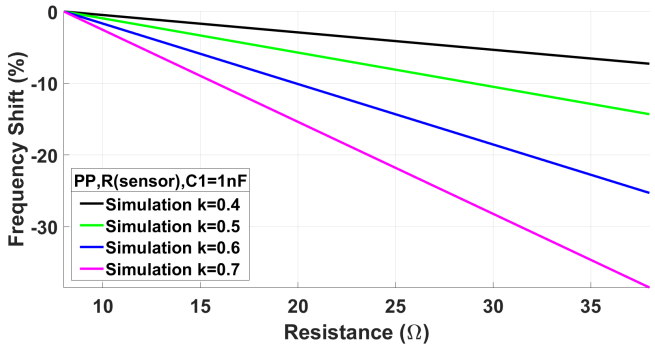

Figure A.4: LTspice simulations for variations in R_{sensor} with the PP topology and $C_1 = 1$ nF. The simulated values for k=0.8 and 0.9 showed unrealistic behaviour and were removed.

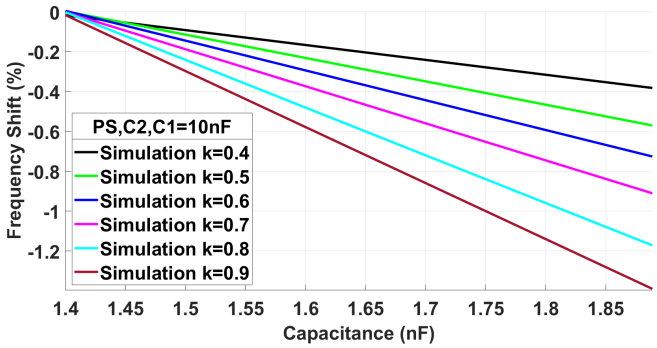

Figure A.5: LTspice simulations for variations in C_2 with the PS topology and $C_1 = 10$ nF.

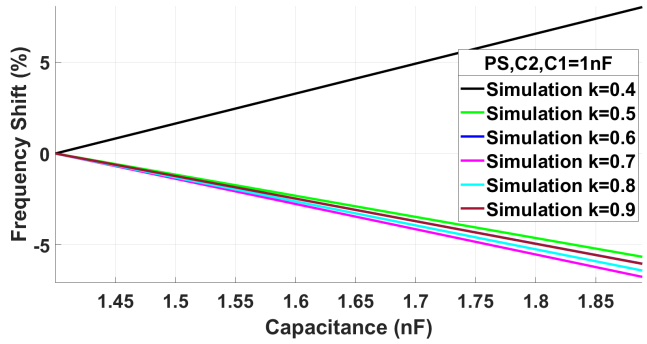

Figure A.6: LTspice simulations for variations in C_2 with the PS topology and $C_1 = 1$ nF.

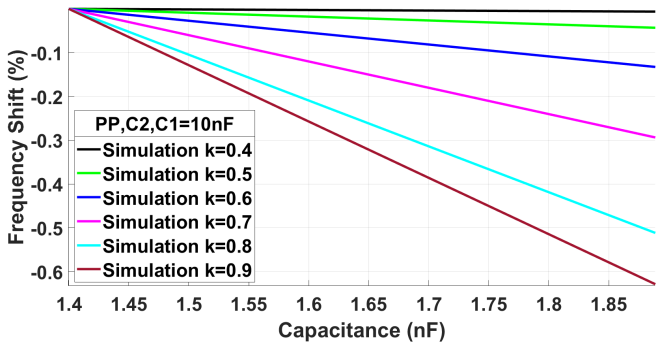

Figure A.7: LTspice simulations for variations in C_2 with the PS topology and $C_1 = 10$ nF.

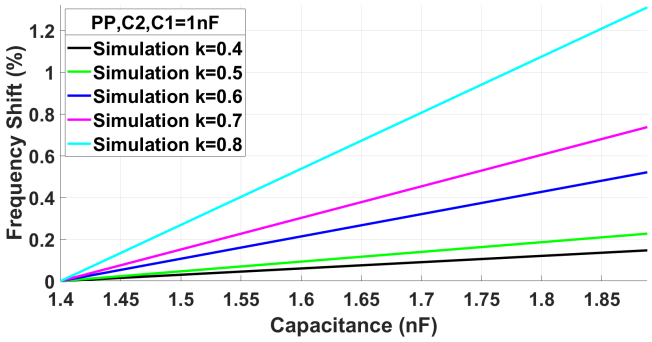

Figure A.8: LTspice simulations for variations in C_2 with the PS topology and $C_1 = 1$ nF. The simulated values for k=0.9 showed unrealistic behavior and were removed.

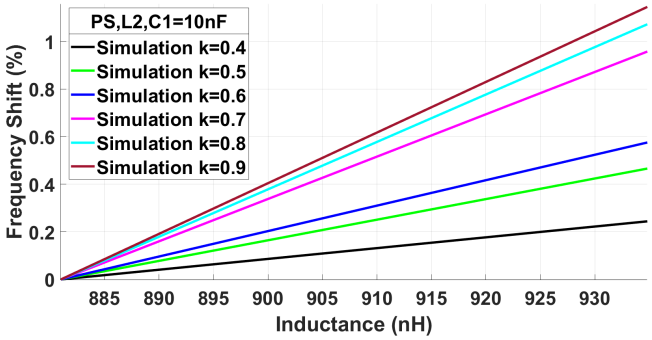

Figure A.9: LTspice simulations for variations in C_2 with the PS topology and $C_1 = 10$ nF.

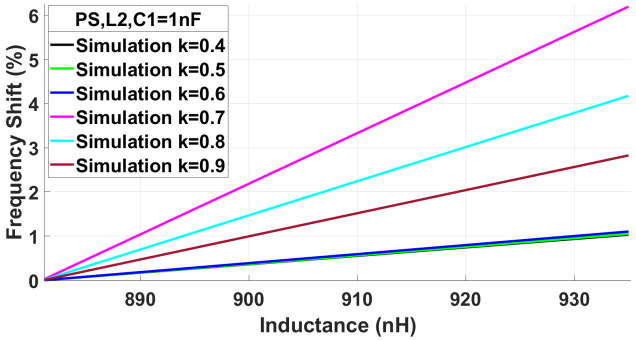

Figure A.10: LTspice simulations for variations in C_2 with the PS topology and $C_1 = 1$ nF.

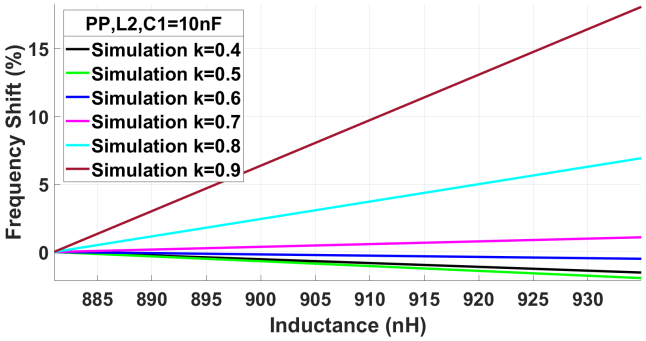

Figure A.11: LTspice simulations for variations in C_2 with the PS topology and $C_1 = 10$ nF.

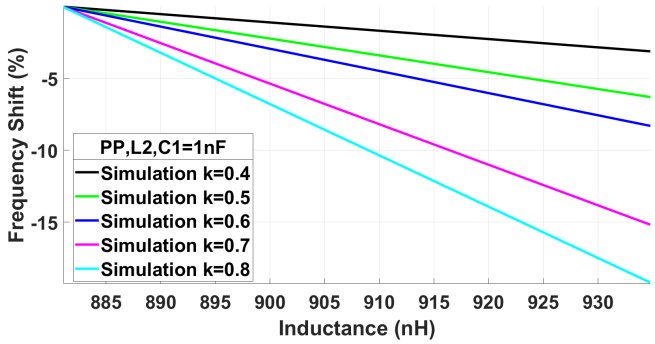

Figure A.12: LTspice simulations for variations in C_2 with the PS topology and $C_1 = 1$ nF.

A.2 Strain Measurement

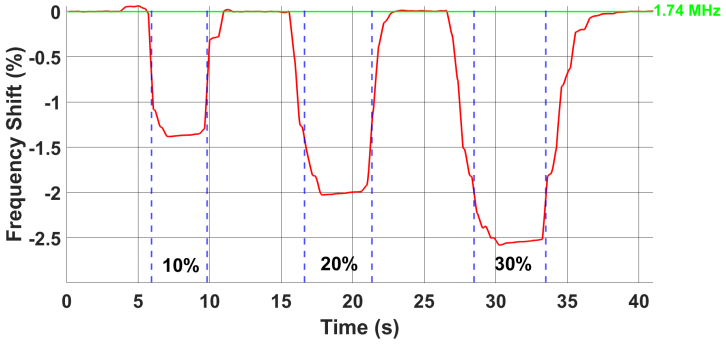

Figure A.13: Systematically induced strain on R_{sensor} with the PP topology and $C_1 = 10$ nF.

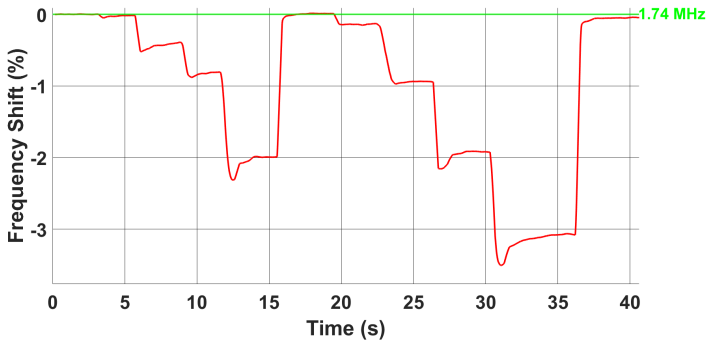

Figure A.14: Actively induced strain on R_{sensor} with the PP topology and $C_1 = 10$ nF.

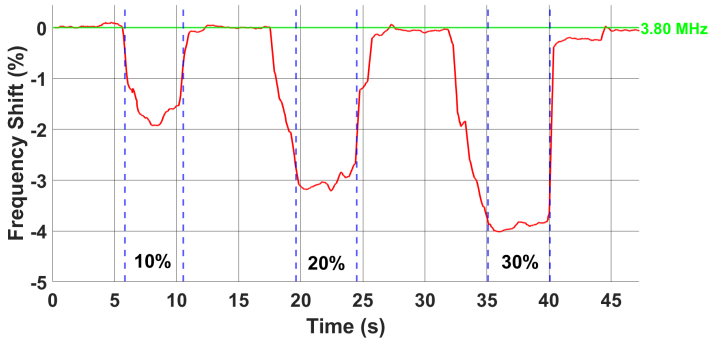

Figure A.15: Systematically induced strain on R_{sensor} with the PP topology and $C_1 = 1$ nF.

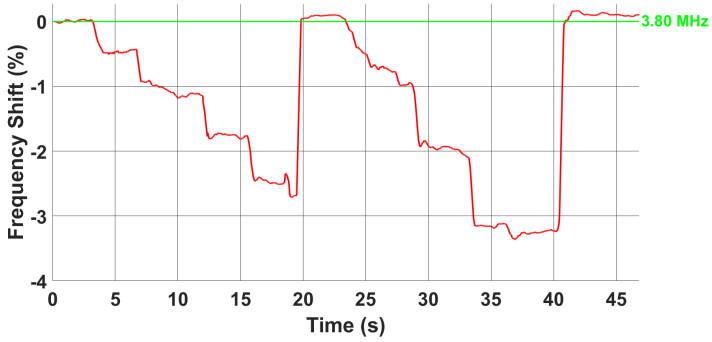

Figure A.16: Actively induced strain on R_{sensor} with the PP topology and $C_1 = 1$ nF.

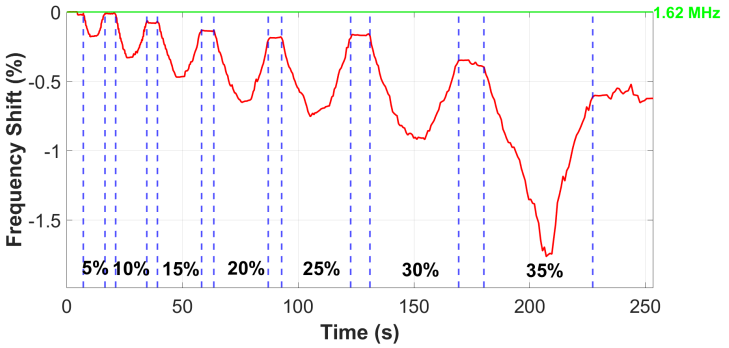

Figure A.17: Systematically induced strain on C_2 with the PS topology and $C_1 = 10$ nF.

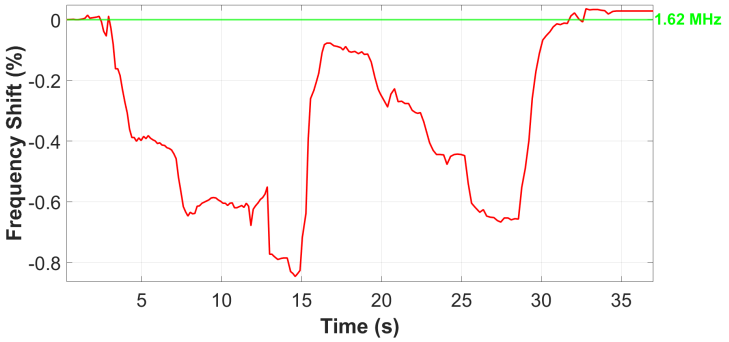

Figure A.18: Actively induced strain on C_2 with the PS topology and $C_1 = 10$ nF.

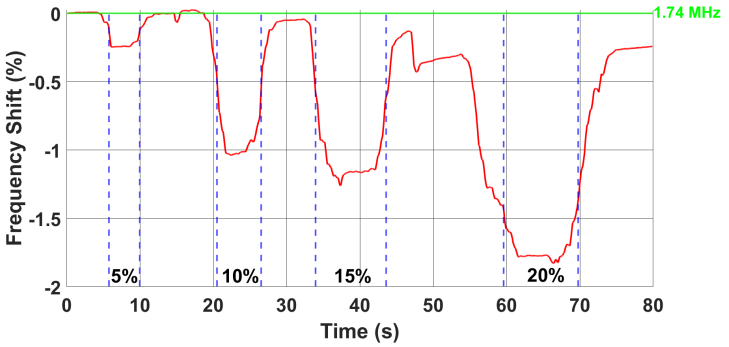

Figure A.19: Systematically induced strain on C_2 with the PP topology and $C_1 = 10$ nF.

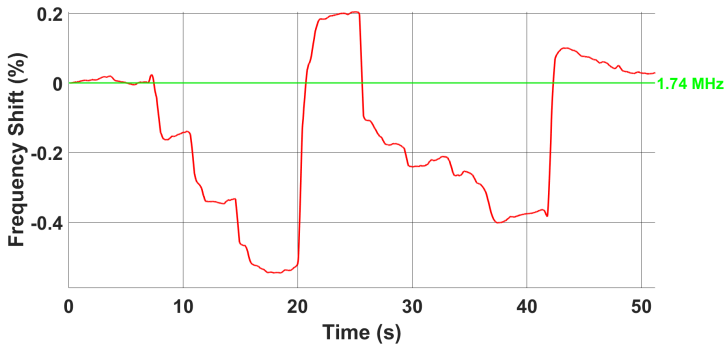

Figure A.20: Actively induced strain on C_2 with the PP topology and $C_1 = 10$ nF.

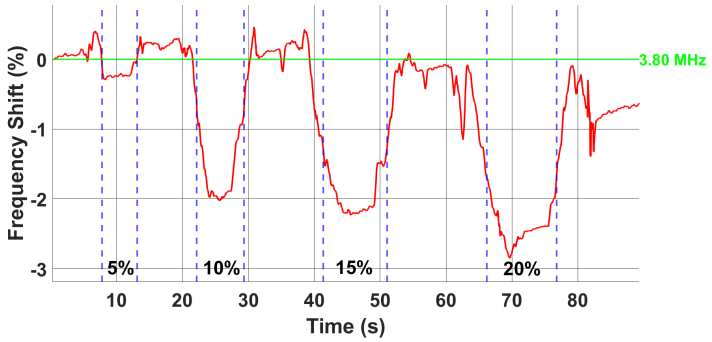

Figure A.21: Systematically induced strain on C_2 with the PP topology and $C_1 = 1$ nF.

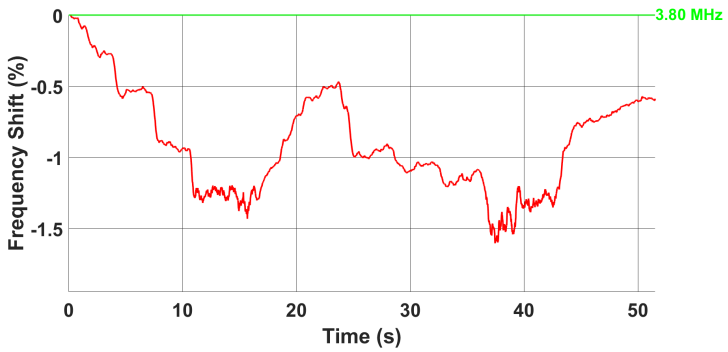

Figure A.22: Actively induced strain on C_2 with the PP topology and $C_1 = 1$ nF.